Alma Mater Studiorum - Università di Bologna

DOTTORATO DI RICERCA IN

FISICA

Ciclo 36

Settore Concorsuale: 02/D1 - FISICA APPLICATA, DIDATTICA E STORIA DELLA FISICA

Settore Scientifico Disciplinare: FIS/07 - FISICA APPLICATA A BENI CULTURALI, AMBIENTALI, BIOLOGIA E MEDICINA

DIFFUSING ALPHA PARTICLES RADIATION TREATMENT OPTIMIZATION IN CLINICAL SETTINGS

Presentata da: Giacomo Feliciani

Coordinatore Dottorato

Alessandro Gabrielli

Supervisore

Gastone Castellani

Co-supervisore

Anna Sarnelli

Esame finale anno 2024

Abstract

Alpha-particle emitters have shown significant therapeutic efficacy and a unique mechanism that can overcome radiation resistance. They cause multiple DNA double-strand breaks along their paths, which can be visualized in both laboratory settings and in living organisms, specifically in human lymphocytes. Alpha particle therapy is used for targeted cancer therapy and bone pain relief. Recent advancements in novel treatments involving ^{224}Ra have shown potential for multipurpose usage, similar to low-dose-rate brachytherapy. A new technique, ^{224}Ra DaRT, employs a decay chain to release short-lived alpha emitting atoms from seeds, particularly ^{220}Rn, which can diffuse in surrounding tissues. This technique extends the "range" of alpha particles from micrometers to several millimeters, leading to complete tumor destruction while preserving nearby healthy tissue.

The diffusion of ^{220}Rn is governed by a constant effective diffusion coefficient, D_{Rn}, and assumes that all ^{220}Rn atoms originate from a singular point source located at the origin. The absorbed dose distribution extends from the source insertion point to infinity, with the diameter exhibiting a pronounced increase at significantly low levels of source activity. The area exposed to alpha particle irradiation is likely to be on the scale of millimeters rather than a few microns. The emission of the third alpha particle, ^{212}Pb, occurs due to the decay of ^{212}Pb progeny, specifically ^{212}Bi and ^{212}Po. Two experimental techniques were employed to ascertain the spatial distribution of ^{212}Pb within treated tumors: gamma spectroscopy and alpha emissions from its progeny, ^{212}Bi and ^{212}Po. Furthermore a biokinetic model was developed and tested with 3 patients treated at our institution.

A feasibility study was conducted from 2017 to 2021 to assess the viability of using ^{224}Ra DaRT seed implantation for treating skin squamous cell carcinomas affecting the skin and head and neck regions. The study found that 48% of patients experienced acute grade 2 toxicity, cured within a month. The positive tolerance outcomes may be attributed to the highly precise dosage distribution achieved using the DaRT technique. The treatment achieved a tumor complete response rate of 75%.

The abscopal effect (AE) is a sporadic event of tumor regression following radiotherapy treatment observed at a distance from the irradiated site was observed in one of the patients treated with DaRT. The mechanism underlying adverse events linked to an increased immune response triggered by high-dose radiation remains poorly defined and unclear. The abscopal effect is the subject of numerous theories, including leukemias and lymphomas, local irradiation of solid tumors, immune-mediated effects, and "in vivo vaccination." Radiation therapy can function as an immunostimulant, releasing danger signals and producing immunogenic cell death. DaRT treatment, which uses high-LET alpha particles for in situ tumor ablation, may be significant due to its ability to trigger an anti-tumor immune response more easily than low-LET radiation. This could provide new opportunities for DaRT in clinical settings where radiation therapy is typically ineffective.

In this thesis we extensively report an abscopal effect observed in a patient treated with DaRT.

Furthermore we discuss improvements to DaRT technique in particular we endeep how to use an external radio-opaque template in the Diffusing Alpha-emitters Radiation Therapy (DaRT) technique's pre-planning and treatment stages. This device would help to determine the proper number of sources for tumour coverage ac-counting for subcutaneous invasion and augmenting DaRT safety. The procedure will be carried out in a first phase on phantom and then applied to a clinical case. A typical DaRT procedure workflow comprises steps like tumor measurements and delineation, source number assess-ment, and therapy administration. As first step an adhesive fiberglass mesh (spaced by 2 mm) tape was applied on the skin of the patient and employed as frame of reference. A Physician contoured the lesion and marked the entrance points for the needles with a radio opaque ink marker. According to the radio opaque marks and metabolic uptake the clinical target volume was defined and with a commercial brachytherapy TPS it was possible to simulate and adjust the spatial seeds distribution. After the implant procedure a CT is performed again to check the agreement between simulations and seeds positions. With the procedure described above it was possible to simulate a DaRT procedure on phantom in order to train physicians and subsequently apply the novel approach on patient outlining the major issues involved in the technique. The present work innovates and supports DaRT technique for the treatment of cutaneous cancers improving its efficacy and safety.

Prostate cancer is the second most common cancer among males globally, accounting for nearly two-thirds of all cases. Advances in radiotherapy improve targeting and dose, but biochemical failure remains a challenge. Salvage therapies, such as SRP, brachytherapy, cryotherapy, and HIFU, have varying toxicities and complication rates. DaRT seeds offer a new potential salvage treatment to treat prostate cancers with alpha particle-based interstitial radiation devices. However, precision and accuracy of seeds insertion are crucial due to the small range of alpha particles in tissue. Potential pitfalls of DaRT technique are discussed in this thesis together with solutions that may be undertaken.

In the end we conclude that for numerous years, brachytherapy has heavily depended on the use of radioactive beta and gamma sources however, the introduction of novel sources with enhanced radio-biological potency holds significant potential in offering substantial advantages to patients afflicted with solid tumors that have a bleak prognosis. Additional studies are currently being conducted to assess the feasibility and safety of DaRT therapy in the treatment of various solid tumors, including pancreatic tumors, as well as recurring breast, prostate, and vulvar malignancies.

a Bea,
nel vento tacevano le parole,
che insieme a te,
ora suonano l'amore.

Diffusing alpha particles radiation treatment optimization in clinical settings

Summary

Chapter 1 Diffusing alpha particles Radiation Therapy (DaRT) foundations

1.1 Introduction to alpha particle treatments

Alpha-particle emitters possess significant therapeutic efficacy and exhibit a fundamentally innovative mechanism. These emitters are capable of potentially overcoming radiation resistance due to the unique characteristics of the alpha particles they emit, namely their limited range (50-100 mm) and high linear energy transfer (LET). Alpha particles cause multiple DNA double-strand breaks along their paths. The study conducted by Eberlein et al. [1–4] demonstrates the ability to observe the repair of double-strand breaks in DNA caused by beta-emitting radionuclides. This repair process can be visualized both in laboratory settings (in vitro) and within living organisms (in vivo), specifically in human lymphocytes. The visualization is achieved through the use of the g-H2AX assay. Figure 1 depicts the trajectory of an alpha particle as it traverses a lymphocyte in the human body, thus demonstrating the applicability of this assay to alpha emitters as well.

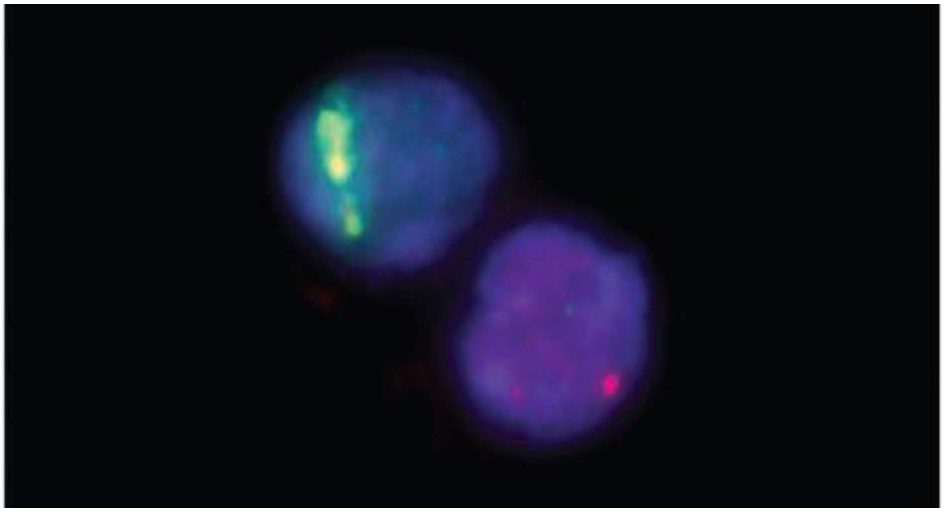

Figure 1 DNA damage caused by the track of an alpha particle (shown as a green streak) through a human lymphocyte visualised by the g-H2AX assay (image courtesy of H. Scherthan, Bundeswehr Institute of Radiobiology, Munich, Germany).

The two major uses of alpha particle therapy are for targeted cancer therapy and the relief of bone pain. Sgouros et al [5] provide descriptions of examples pertaining to targeted cancer therapy. These examples encompass the potential applications of utilizing ^{213}Bi-labelled antibodies for the treatment of melanoma or leukaemia, as well as the use of ^{211}At-labelled antibodies for the treatment of ovarian carcinoma. Using ^{225}Ac- or ^{213}Bi-

PSMA ligands to treat metastatic prostate cancer is one recent example by Kratochwil et al [6]. According to Parker et al. [7], ^{223}Ra dichloride has been granted permission to be marketed in Europe and the USA as the first and only alpha emitter for the purpose of palliating metastatic bone pain. This treatment is specifically intended for patients diagnosed with castration-resistant prostate cancer and experiencing symptomatic bone metastases. All previously conducted investigations documented in the existing body of literature [5, 6] were conducted at a single research facility and primarily involved compassionate use applications. These studies are not conducive to establishing overarching guidelines for the utilization of alpha emitters in patient treatment or formulating comprehensive radiation protection protocols. In recent times, there have been advancements in novel treatments involving the use of ^{224}Ra. These treatments have been developed in two phase 1 trials, where ^{224}Ra is either adsorbed to calcium carbonate microparticles for intraperitoneal therapy or electrochemically deposited on stainless steel or titanium seeds. These last treatments have shown potential for multipurpose usage, similar to low-dose-rate (LDR) brachytherapy performed with ^{103}Pd and ^{125}I, and can be utilized for the treatment of various cancers such as skin, prostate, pancreatic, and head and neck cancers. The examination of this recent application will serve as the central focus of this doctoral thesis.

1.1.1 An overview of ^{224}Ra DaRT

A new technique firstly described by Arazi et al in 2007 [8] which employs ^{224}Ra elettrochemically deposited on for the treatment of tumours has been recently implemented in our institution. ^{224}Ra decay chain continually release short lived alpha emitting atoms from seeds surface and in particular ^{220}Rn which has gaseous properties and is able diffuse in the surrounding tissues migrating distant from the implanted source seed. These atoms spread within the tumor by the combined effects of diffusion and convection (vascular and possibly interstitial), forming a region of tumor cell destruction, where a lethal dose is delivered through their alpha decays. Since, as in direct intratumoral injection, the alpha emitters begin their journey in the cellular space, rather than being conjugated to macromolecules that arrive at the tumor in the blood, and since no molecular targeting mechanism is involved, their subsequent distribution throughout the tumor may be expected to be less affected by obstacles.

This is the fundamental characteristic for the efficacy of the technique because extend the “range” of alpha particles from micrometers to several millimetres. Coverage of the lesion volume with these radioactive seeds would then lead to complete destruction of the tumour while preserving the nearby healthy tissue.

1.1.2 ^{224}Ra alpha emitter release concept

The atoms undergoing diffusion are released from the source through a process known as recoil. This occurs when a radioactive atom emits an alpha particle in a specific direction, carrying an energy range of 6-9 MeV. Consequently, the daughter atom undergoes a recoil effect, moving in the opposite direction with a kinetic energy of approximately 100-170 keV. The magnitude of this energy is significant enough to enable the recoiling atom to travel a distance of approximately 10-20 nm within the majority of solid materials. Therefore, the source is comprised of parent alpha-emitting atoms that are situated in close proximity beneath its surface. These atoms are positioned at a depth that prevents them from directly entering the tumor, but facilitates the substantial release of their recoiling daughters. The aforementioned entities exhibit a recurring pattern of retracting towards the neoplasm, with a rate of retreat that diminishes exponentially in accordance with the half-life of the progenitor isotope.

1.1.3 ^{224}Ra Decay Chain

In order to implement the proposed concept, DaRT utilizes the alpha decay chain originating from ^{224}Ra, as depicted in figure 2. The source, which consists of a thin conducting wire containing a modest quantity of ^{224}Ra, is carefully introduced into the tumor using a needle with a fine gauge. Upon entering the tumor, the source undergoes a process influenced by the half-life of ^{224}Ra (3.66 days), during which it emits ^{220}Rn (with a half-life of 55.6 seconds), ^{216}Po (with a half-life of 0.15 seconds), and ^{212}Pb (with a half-life of 10.64 hours) atoms through recoil. The remaining atoms of ^{224}Ra remain beneath the surface. The noble gas ^{220}Rn exhibits diffusion within the extra- and intra-cellular regions adjacent to its origin, free of any chemical interactions. It occasionally permeates the porous network of blood vessels within tumors, both entering and exiting. The decay of ^{220}Rn results in the emission of two alpha particles, both originating from the decay of ^{216}Po, a daughter isotope with a very short half-life. The disintegration of ^{216}Po occurs near the original decay event of ^{220}Rn. The introduction of ^{212}Pb into the tumor occurs through two mechanisms: direct recoil from the source or as a result of the decay of ^{216}Po, which subsequently produces a third alpha particle. Following this, ^{212}Pb undergoes beta decay with a half-life of 60.6 minutes, resulting in the formation of ^{212}Bi. ^{212}Bi can then undergo either alpha decay with a half-life of 3.05 minutes, leading to the production of ^{208}Tl, or beta decay with a half-life of 0.3 microseconds, resulting in the formation of ^{212}Po. Finally, ^{212}Po undergoes alpha decay to yield stable ^{208}Pb [9].

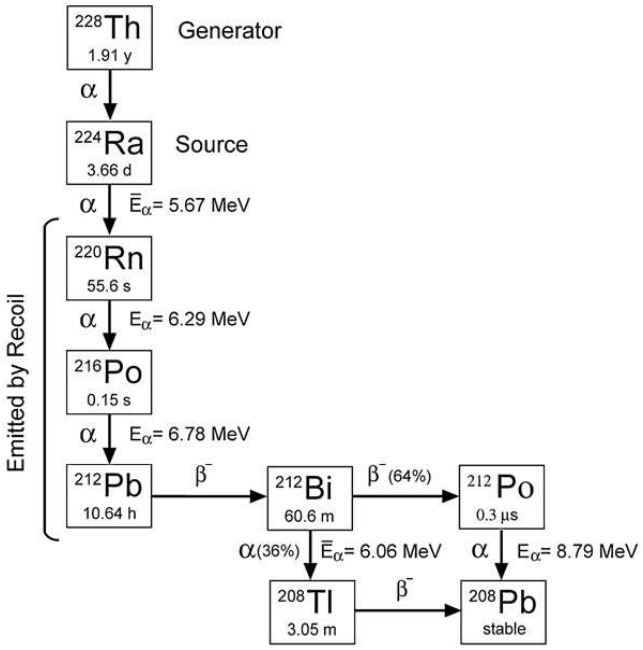

Figure 2 The 224Ra decay chain.

The production of ^{224}Ra-bearing sources relies on the utilization of a ^{228}Th generator, which consists of a surface coated with a layer containing ^{228}Th. This is because ^{224}Ra is produced through the alpha decay of ^{228}Th, which has a half-life of 1.91 years. The layer of ^{228}Th on the generator surface is designed to be thin enough to allow for the significant release of recoiling ^{224}Ra atoms. The experimental configuration, as depicted in Figure 3, consists of a physically separated enclosure filled with air. At one end of the enclosure is the ^{228}Th generator, while at the other end is a conducting wire that functions as the injected source. The wire is maintained at a negative potential in relation to the generator, resulting in the convergence of electrostatic field lines originating from the generator surface in close proximity to its tip. The ^{224}Ra ions, which possess positive charge, recoil out of the generator and exhibit energies of approximately 100 keV. These ions rapidly undergo thermalization through collisions with air molecules. Subsequently, they drift along the field lines until they reach the wire, where they ultimately settle on its surface. In order to prevent the removal of the highly reactive radium from the wire upon insertion into tissue, a subsequent heating process is employed. This heating process induces the diffusion of radium away from the wire's surface to a depth of several nanometers. Despite this diffusion, a significant release of the alpha emitting daughters still occurs. The electrostatic collection stage, which is determined by the half-life of ^{224}Ra at 3.7 days, typically lasts for a few days.

Chapter 2 Methods in 224-Ra source preparation and experimental measurements

2.1 ^{224}Ra Source preparation

The ^{228}Th generators were fabricated through the process of evaporating a droplet of carrier-free 1M hydrochloric acid (HCl) solution, which contained a maximum of 370 kBq of $^{228}ThCl_4$ obtained from Isotope Products Laboratories in Burbank, CA, USA. This evaporation was performed on a hydrophilic silicon surface with an area of 4 cm^2. Subsequently, the silicon surface was subjected to heating in a vacuum environment at a temperature of 800 ˚C shown in Figure 3. The experimental results demonstrated the formation of ^{228}Th layers, wherein the probability of desorption of ^{224}Ra was found to be between 20% and 30%. This implies that for each decay event of ^{228}Th, there was a corresponding probability of 20% to 30% for the recoiling ^{224}Ra atom to detach from the surface. The activities of ^{228}Th were quantified using a standard solid state alpha particle spectroscopy technique. The desorption probability of ^{224}Ra was determined through the measurement of the accumulation of ^{224}Ra on a stainless steel foil positioned near the ^{228}Th generator within a vacuum environment.

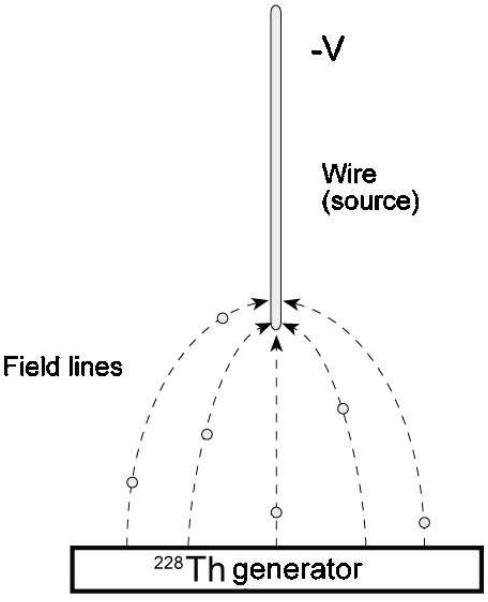

Figure 3 Schematic representation of the generator–source setup.

For the in vivo experiments described below, sources consisting of acupuncture needles made of stainless steel with a diameter of 0.3 mm were prepared using the procedure mentioned above. The standard voltage for collection ranged from 2 to 3 kilovolts (kV), while the typical distance between the ^{228}Th generator and the wire tip was between 5 and 15 millimeters (mm). As a result, the collection efficiency of ^{224}Ra was approximately 95%. The wires were subjected to a temperature of 450 ◦C in a N_2 atmosphere after being loaded with ^{224}Ra. The wires were then analyzed using standard alpha spectroscopy. Subsequently, the wires were immersed in water multiple times and re-evaluated until the amount of radium lost to the water reached an acceptable level, which was typically around 1-2% of the initial source activity. Subsequently, the wires were trimmed to achieve a definitive length of 6 mm. The activities of sources containing ^{224}Ra varied between 10 and 130 kBq, while the desorption probabilities of ^{220}Rn ranged from 30% to 43%.

2.2 ^{220}Rn diffusion—theoretical consideration

The physical viability of DaRT can be understood by examining the diffusion of ^{220}Rn, which determines the distribution of radiation dose associated with the initial emission of two alpha particles from the source. The inert characteristics of radon allow for the estimation of the dose profile resulting from its migration through the use of a simple theoretical model. It is postulated that the movement of ^{220}Rn is exclusively governed by diffusion, characterized by a constant effective diffusion coefficient, D_{Rn}. Additionally, it is assumed that all ^{220}Rn atoms originate from a singular point source located at the origin, and their activity diminishes exponentially over time in accordance with the half-life of ^{224}Ra. The local activity of ^{220}Rn at any given point can be determined for all times by solving the time-dependent diffusion equation under the conditions outlined in appendix A of Arazi et al [8]. The absorbed dose distribution, which extends from the source insertion point to infinity, can be estimated by integrating the local activity over time. This estimation assumes that each decay of ^{220}Rn results in the deposition of energy locally by two alpha particles, with one contributed by ^{220}Rn and the other by ^{216}Po. Although this approach actually provides the local kerma rather than the absorbed dose, for the purpose of this discussion, we will disregard the distinction between the two. In the absence of published data on the effective diffusion coefficient of radon in tissue, we relied on two established reference values. Firstly, we utilized the diffusion coefficient of radon in water at a temperature of 37 ◦C, which was reported as 1.9 × 10−5 cm^2 s^{-1} by Jahne et al in 1987. Additionally, we considered the effective diffusion coefficient of xenon in tissue, as recommended by the NRC report on radon in drinking water in 1999, which was estimated to be 0.5 × 10−5 cm^2 s^{-1}. In the subsequent analysis, we opt for a reference dose of 10 Gy to ascertain the extent of the region impacted by the source. In Figure 4 (left), the absorbed dose of ^{220}Rn/^{216}Po is presented for a point source. The initial release rate of

^{220}Rn at t = 0 is 37 kBq (1 μCi). The absorbed dose is calculated for two different values of the effective diffusion coefficient. When the value of D_{Rn} is 1.9×10−5 cm^2 s^{-1}, the absorbed dose surpasses 10 Gy within a radial distance of 2.6 mm from the source. Conversely, when D_{Rn} is 0.5×10−5 cm^2/s, the absorbed dose reaches this threshold up to a distance of 1.7 mm from the source. Figure 4(right) illustrates the correlation between the distance and the initial release rate of the source ^{220}Rn, while maintaining consistent diffusion coefficient values. The diameter exhibits a pronounced increase at significantly low levels of source activity, followed by a more gradual incline for sources with higher levels of activity. Taking into consideration that the decay of ^{220}Rn serves as the initial stage for the migration of ^{212}Pb, which can disperse away from the source, a straightforward calculation indicates that the area exposed to alpha particle irradiation is likely to be on the scale of millimeters rather than a few microns. The subsequent section presents an empirical validation of this proposition.

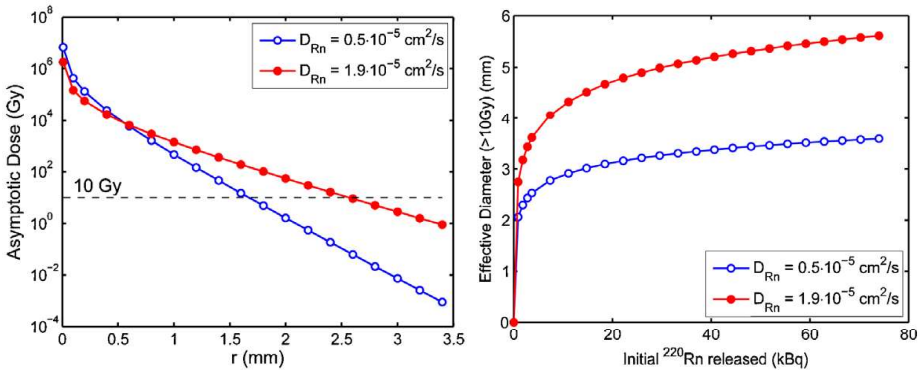

Figure 4 Results of simple diffusion calculations regarding the asymptotic dose delivered by^{220}Rn and 216Po away from a point source at the origin, for two reference values for radon's effective diffusion coefficient. (left) The dependence of the dose on the radial distance from a source releasing 37 kBq ^{220}Rn at t = 0. (right) The dependence of the diameter of the region receiving >10 Gy asymptotically on the source ^{220}Rn release rate.

2.3 In vivo measurements of ^{212}Pb/^{212}Bi distributions

The emission of the third alpha particle occurs as a consequence of the decay of ^{212}Pb progeny, specifically ^{212}Bi and ^{212}Po. In order to approximate this particular element of the overall dosage, it is imperative to initially examine the transportation of ^{212}Pb within the tumor, followed by an assessment of the potential redistribution of ^{212}Bi in relation to ^{212}Pb. In contrast to radon, ^{212}Pb exhibits chemical interactions with adjacent molecules, specifically lead-binding proteins [10]. The subsequent dissemination of these proteins within the tumor is regulated by their intracellular transport, as well as their distribution within the extracellular space and the vascular network. Proteins labeled with ^{212}Pb, along with potentially free ^{212}Pb ions, that enter the plasma can either be sequestered by red blood cells or remain accessible for interaction with the surrounding tissue [11]. The

transportation of ^{212}Pb through viable vascular pathways allows for its removal from the tumor and subsequent redistribution across multiple organs. This intricate image seemingly challenges the feasibility of quantitative theoretical modeling. However, in contrast to ^{220}Rn, which has a half-life that is too brief to permit direct determination of its in vivo distribution, the half-life of ^{212}Pb is conveniently lengthy, allowing for the possibility of conducting such measurements. Two experimental techniques were employed to ascertain the spatial distribution of ^{212}Pb within treated tumors. One method involved the utilization of gamma emissions, while the other method involved the utilization of alpha emissions from its progeny, namely ^{212}Bi and ^{212}Po. The technique of gamma spectroscopy was employed to assess the local activity ratio of ^{212}Bi/^{212}Pb within the tumor, as well as to quantify the leakage of ^{212}Pb from the tumor and its subsequent accumulation in different organs.

Experimental tumor model

The study conducted by Blank et al. [12] involved the assessment of ^{212}Pb and ^{212}Bi distributions within murine squamous cell carcinoma (SCC) tumors. These tumors were derived from the SQ2 cell line, which originated from a spontaneous SCC tumor in a male BALB/c mouse. In order to obtain measurements, in vivo techniques were employed. The cells were cultured in Dulbecco's Modified Eagle Medium (DMEM) supplemented with 10% fetal calf serum, 2 mM L-glutamine, 100 U/ml penicillin, and 100 µg/ml streptomycin, all of which were obtained from Biological Industries located in Beit Haemek, Israel. Male BALB/c mice, aged 8-12 weeks, were procured from the breeding colony located at Tel Aviv University in Israel. The animals were subjected to intracutaneous inoculation with 5×10^5 SQ2 cells in 0.2ml of HBSS buffer (Biological Industries, Beit Haemek, Israel) at the low lateral region of the back. A solitary wire source containing ^{224}Ra was introduced into the system between 7 to 20 days following the inoculation of tumor cells, during a period when the average lateral diameter of the tumor ranged from 6 to 15 mm. The procedure of wire insertion was conducted using conventional 2.5 mL syringes equipped with 23G needles. The wires were inserted into the needle tip and carefully positioned within the tumor center using an internally placed plunger along the axis of the syringe. The animal care and experimentation procedures adhered to the guidelines set forth by Tel Aviv University. Anesthesia was administered for all surgical and invasive procedures.

^{212}Pb distribution inside the tumor—tumor dissection experiments

The primary approach for ascertaining the spatial arrangement of ^{212}Pb within a treated tumor involves the dissection of the tumor into numerous small fragments with predetermined masses. These fragments are subsequently measured individually using a gamma counter. The aforementioned experimental protocol was conducted on a cohort of ten squamous cell carcinoma (SCC) tumors. Each tumor was subjected to treatment using a solitary source. This intervention was administered when the tumors' collective average lateral diameter ranged from 8 to 15 millimeters. The tumors were surgically excised 2-4 days following source insertion. Subsequently, they were preserved by

freezing in dry ice with acetone and then dissected into vertical slices of approximately 2 mm thickness using surgical blades. The slices were divided into smaller pieces ranging from 5 to 15 mg, ensuring that the spatial arrangement was maintained and cross contamination of activity was avoided. Blades were regularly replaced during this process. The complete set of samples, usually consisting of 100-200 pieces, was subsequently assessed using a well-type NaI gamma counter (LKB Wallac 1282 CompuGamma, Wallac, Finland), with specific attention given to the ^{212}Pb 239-keV line.Multiple measurements were conducted for each sample during a standard timeframe of 24 to 72 hours. Given the presence of a 241-keV (4.1%) gamma line in ^{224}Ra, which cannot be distinguished from the ^{212}Pb 239-keV line (43.6%) using the Wallac detector, the data exhibiting time-dependence were subjected to a fitting process. This fitting involved employing a linear combination of two exponential functions, each corresponding to the half-lives of ^{224}Ra and ^{212}Pb, respectively. The purpose of this fitting was to accommodate the potential existence of ^{224}Ra in the sample.The specific activity of ^{212}Pb exhibited a pronounced peak in close proximity to the source, decreasing by approximately two orders of magnitude within a range of 2-3 mm. Figure 5 depicts the cumulative fraction of ^{212}Pb in relation to the cumulated mass of tumor cuts, which have been sorted based on the descending order of ^{212}Pb specific activity. This average is calculated from the data obtained from ten dissected tumors. It should be noted that while the majority of ^{212}Pb is concentrated within a few dozen milligrams, there exists a significant proportion of activity that is distributed at greater distances from the source. As an illustration, it has been observed that a proportion of 10% of the overall ^{212}Pb activity is detected beyond the central 200 mg area surrounding the source. The measured quantity of ^{224}Ra activity observed in the dissected tumors was determined to be less than 1% of the original ^{224}Ra source activity.

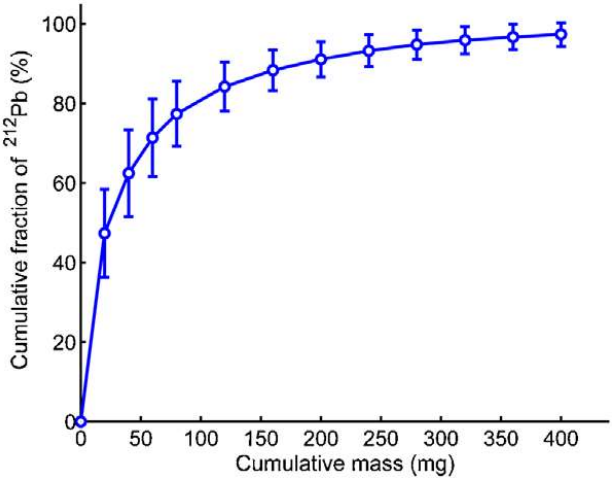

Figure 5 The findings from the tumor dissection experiments revealed the relationship between the cumulative fraction of ^{212}Pb present within the tumor and the cumulative mass of tumor cuts. These results were obtained by averaging the data collected from the dissection of 10 squamous cell carcinoma (SCC) tumors. The tumor samples were arranged in descending order based on their specific activity of ^{212}Pb. Error bars are graphical representations that indicate the standard deviations.

^{212}Pb autoradiography using a Fuji phosphor-imaging plate

One benefit of the dissection procedure is that it makes measuring the average ^{212}Pb activity in each tumor cut simple. Nevertheless, the resulting spatial resolution is only approximately 2 mm. Autoradiography measurements of ^{212}Pb in histological tumor cuts on a Fuji phosphor-imaging plate can be used to provide a 10-fold increase in resolution [13]. It should be noted that this approach primarily records the alpha decays of ^{212}Bi and ^{212}Po, which are created by and in localsecular equilibrium with ^{212}Pb, rather than directly detecting ^{212}Pb itself. The beta decays of ^{212}Pb only contribute somewhat to this process. Ten SCC tumors in the tests were treated with a single source once they had grown to a size of 6–15 mm. The tumors were removed and the source was eliminated 5-7 days later. Tumors that had been removed were left in 4% formaldehyde for 24, 36, or 48 hours.

Standard protocols were followed in the processing and paraffin embedding of the preserved specimens. Using a Leica RM2055 microtome (Leica, Nussloch, Germany), histological slices (5 or 10 μm) were cut and put on glass slides. After that, the slides were placed atop a 12 μm Mylar foil to shield them from the Fuji image plate (BAS-TR2040S, Fuji Photo Film, Japan) and avoid direct contact with it. Two or three hours and then roughly fifteen hours were spent measuring the slides twice. In several instances, a follow-up measurement was taken a day later. After every measurement, a Fuji FLA-2000 system with 100 or 200 μm pixel size scanned the plate. Hematoxylin-Eosin (H&E) (Surgipath, Richmond, IL, USA) was subsequently used to stain the tissues in order to detect tissue damage and connect the results with the activity distribution data. The point spread function (PSF) of the imaging plate and the real activity patterns in the histology samples are combined to create the images that are obtained by scanning the plate [14, 15]. There is some spreading as a result, however this can be fixed by using deconvolution algorithms, which often call for PSF knowledge. Using the Lucy-ichardson technique [16, 17] included in MATLAB's image processing toolbox, the recorded pattern was deconstructed in our instance. The process used a point-like ^{212}Pb sample and depended on independent measurements of the imaging plate PSF. By using a dual-exponent fit, the ^{224}Ra/^{212}Pb activity ratio in the histology sample was estimated from consecutive observations of a particular section. Using ^{212}Pb calibration samples of known activities measured simultaneously with the histological sections, the deconvoluted image was translated pixel-by-pixel to local ^{212}Pb activity (at the moment the measurement began). Rather than assuming pure ^{212}Pb temporal behavior, the local ^{212}Pb activity at the moment of tumor removal was assessed by back-extrapolation using the predicted ^{224}Ra/^{212}Pb ratio. Analysis of the recorded images revealed that ^{212}Pb activities were sharply peaked near the source insertion point, with significant local activities extending over a region of several millimeters; the migration of ^{212}Pb inside the tumor (for sources placed near its center) was not isotropic, but anisotropy effects were generally not very large. The activity

pattern seemed to move toward the edges of the tumor in numerous instances. The direction of the cutting process or the section's placement on the imaging plate had no bearing on the activity patterns that were seen; they were uniform across adjacent sections. 24–48 hours after the tumor was removed, the analyzed samples showed ^{224}Ra activity that was usually just a small percentage of the measured ^{212}Pb activity. As in the tumor dissection studies, the equivalent ^{224}Ra/^{212}Pb activity ratio was at most 1% at the time of tumor excision.

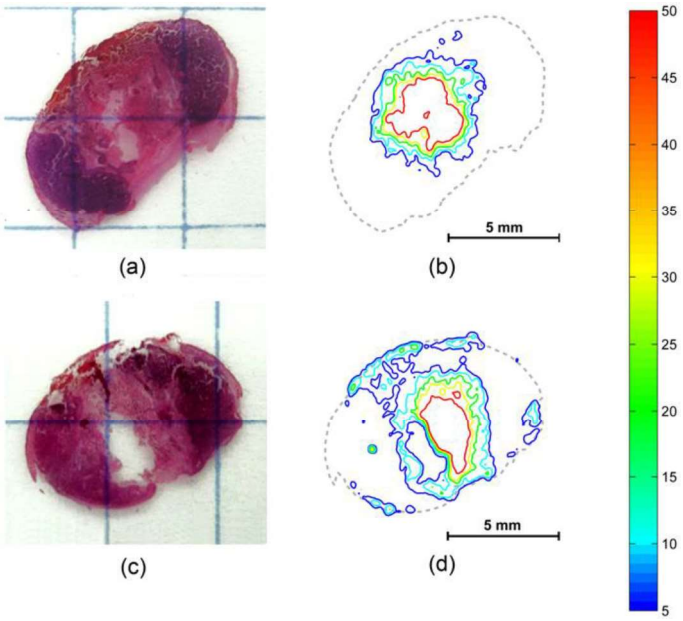

Figure 6 Calculated absorbed dose distributions, based on autoradiography measurements with a Fuji phosphor-imaging plate, compared to tissue damage in 10 µm H&E-stained histological sections taken from two SCC tumors. The scale refers to the alpha particle dose delivered by ^{212}Bi and ^{212}Po from source insertion until tumor removal (Gy). The dose curves shown; 5, 10, 20, 30 and 50 Gy.

The ^{212}Bi/^{212}Po absorbed dose calculation

In order to approximate the local dose resulting from the alpha decays of ^{212}Bi and ^{212}Po from the time of source insertion to a specific point in time (such as tumor excision or infinity), we utilized a simplified methodology, relying on the following assumptions: (1) The biological conditions influencing the movement of diffusing atoms stay constant throughout the treatment process. (2) The temporal dependence of ^{212}Pb at any given place within a tumor is independent of its distance from the source. (3) Both ^{212}Bi and ^{212}Pb exhibit identical distributions.

Based on the given assumptions, it is possible to calculate the local ^{212}Pb activity at any given time, denoted as $\Gamma_{Pb}^{j}(\mathrm{t})$ (where j represents an index indicating the specific tumor section or 'voxel'), using a solitary measurement $\Gamma_{Pb}^{j}(\mathrm{t}_r)$ taken at the moment of tumor

extraction (see to appendix B of Arazi et al [8]). The implication of neglecting the redistribution of ^{212}Bi is that each decay of ^{212}Pb results in the presence of a single alpha particle (either ^{212}Bi or ^{212}Po) at the exact same place. Therefore, the local absorbed dose (or kerma, as previously mentioned) caused by alpha decays of ^{212}Bi/^{212}Po from the time of source insertion until time t, at the specific volume element j, can be expressed as

$$Dose^{j}_{BiPo}(t) = \frac{E_{BiPo}}{m_j} \int_0^t \Gamma^{j}_{Pb}(t')\, dt' \qquad (1)$$

where E_{BiPo} represents the average kinetic energy of the alpha particle emitted by either isotopes (7.8 MeV), and m_j denotes the mass of the jth tumor element. In the Fuji autoradiography studies, the mass of the 'voxel' was determined by making the arbitrary assumption of a tissue density of 1.05 g/cm^3. This assumption was used in conjunction with the pixel area and nominal section thickness to calculate the volume. The absorbed dose was determined by either considering the period from source insertion to infinity (referred to as asymptotic dose) or from source insertion till tumor excision. A rough comparison was made between the estimated absorbed dosage and the observed tissue damage by superimposing the computed isodose curves of a specific histological section onto a scaled image of the corresponding slice, following H&E staining. Figure 6 illustrates the juxtaposition of the measured isodose curves and H&E-staining patterns of selected 10 µm histological sections obtained from the central area of two treated tumors. The initial neoplasm (a), (b) underwent treatment with a 30 kBq ^{224}Ra source, while the subsequent neoplasm (c), (d) was treated with a 72 kBq ^{224}Ra source. The probabilities of ^{220}Rn desorption were observed to be 38% and 40%, respectively. The tumors were surgically excised on the fourth and fifth days, respectively, following the insertion of the source. The color-bar provides a visual representation of the absorbed alpha dosage (in Gy) of ^{212}Bi/^{212}Po at the moment of tumor extraction. Dosage levels beyond 50 Gy are not displayed, as in close proximity to the source, the dose can reach several thousand Gy. Necrotic regions are observed surrounding the site of insertion in both tumors, where the maximum estimated dose is located. The limits of the necrotic zones in the first tumor correspond to a radiation dose of less than 1 Gy, but in the second tumor, the boundaries align with a radiation dose of approximately 5 Gy. Comparative analyses conducted on sections extracted from other tumors, as well as on supplementary sections obtained from the aforementioned two tumors, revealed that the demarcations of the observable necrotic areas aligned with radiation doses spanning from around 1 to 15 Gy. In all instances, a strong visual correlation was observed between the computed dosage and the manifestations of necrosis. It is important to highlight that there was no evidence of cellular damage in the histological sections stained from squamous cell carcinoma (SCC) tumors that were subjected to treatment with inert wires.

2.4 Internal dosimetry Analysis

The preclinical investigation conducted by Arazi et al. [8] and Cooks et al. [18] examined the effects of squamous cell carcinoma (SCC) and lung tumors on mice. The study explored both murine and human-derived tumors and observed significant cell death within a region of several millimetres in diameter. The study conducted by Cooks et al. shown that the use of one or two sources for the treatment of tumors with a diameter of 6-7 mm led to significant inhibition of tumor growth. This treatment approach also resulted in total regression of tumors without any recurrence, hence increasing the overall life expectancy of the subjects. Furthermore, the treatment was found to effectively reduce the occurrence of lung metastases. The effectiveness of the approach was enhanced when it was paired with chemotherapy [19].

The promising outcomes shown in preclinical studies provide a compelling rationale for further exploration of DaRT in clinical environments. Currently, there is ongoing preparation work for a clinical research that is specifically targeting patients with late-stage head and neck squamous cell carcinoma (SCC). This necessitates a comprehensive evaluation of the safety implications associated with the suggested methodology.

In the context of traditional radiotherapy, the administration of radiation to the tumor is often constrained due to the imperative of minimizing harm to adjacent tissues. In the context of DaRT, it is expected that the radiation field will exhibit a rapid decrease in intensity as the distance from the source increases. This characteristic is projected to result in a tumor dose that is highly concentrated in a specific area, while causing minimum harm to nearby healthy structures. Therefore, the dose administered to distant organs due to radionuclide clearance from the tumor via the bloodstream is a possible constraint in DaRT. The topic under investigation in this study is the focal point.

Theoretically, it is possible for all progeny of ^{224}Ra that are produced from DaRT sources to exit the tumor via the bloodstream and disperse across the entire body. Nevertheless, due to the very brief half-lives of ^{220}Rn and ^{216}Po, it is reasonable to infer that these two radionuclides undergo complete disintegration only within the tumor. In contrast, ^{212}Pb possesses a notably extended half-life, enabling its partial removal from the tumor, particularly in well-vascularized regions that are commonly situated towards the perimeter of the tumor. Consequently, this process results in the transportation of its alpha-emitting progeny, namely ^{212}Bi and ^{212}Po. Regarding ^{224}Ra, the generation technique of the DART source imposes restrictions on the shedding of ^{224}Ra activity from the source. This shedding is limited to a minimal proportion of the overall source activity, specifically less than about 0.5%. Therefore, the significance of this effect is minimal and will not be taken into account in this context. After seeing the contrasting macroscopic kinetics of lead in mice and humans, we proceed to employ a theoretical methodology grounded in recognized biokinetic models for lead and bismuth, as well as the Medical Internal

Radiation dosage (MIRD) scheme. This technique allows us to estimate the organ dosage in DART (Direct Alpha Therapy) treatments specifically for humans. The findings from the integrated biokinetic internal dose calculations are subsequently juxtaposed with tolerance dose data in order to assess the potential scope of the DART approach in terms of the maximum permissible ^{224}Ra activity that may be safely delivered to human malignancies.

2.4.1 Theoretical analysis

The kinetics of lead in humans differs significantly from that observed in mice. Specifically, while the blood of mice treated with DaRT therapy includes a small percentage of the total lead activity outside of the tumor, approximately 55% of intravenously administered lead is known to be present in the blood of people [11]. Therefore, in order to calculate the dosages of organs in potential future DART treatments, we employ a theoretical methodology that relies on well-established biokinetic models for human subjects. The preclinical data obtained from mice provides evidence that ^{212}Pb does exit the tumor through the bloodstream. Furthermore, it is observed that the extent of leakage is influenced by the size of the tumor, or more specifically, the proximity between the radiation source and the vascularized regions near the outer edges of the tumor. Additionally, the data indicates that ^{212}Bi and ^{212}Pb exhibit a state of secular equilibrium within the tumor at a macroscopic level. The outcomes of the biokinetic calculations, specifically related to the isotopes ^{212}Pb, ^{212}Bi, ^{212}Po, and ^{208}Tl, are afterwards employed. This is done after a meticulous assignment of cumulated activities to individual organs. These results serve as input for a dosimetric calculation, which follows the MIRD scheme as outlined by Stabin [20].

2.4.2 Biokinetic model

The estimation of internal dosimetry for DART is dependent on the utilization of age-specific biokinetic models for lead and bismuth, which have been developed by the International Commission on Radiological Protection (ICRP). These models are constructed using a combination of data from various sources, including experimental studies, long-term balance studies, and autopsy measurements conducted on both humans and large animals [11, 21]. The current study used a model that specifically targets adults, but it may be readily expanded to encompass individuals of all age groups by incorporating the parameter values outlined in ICRP Publication 67.

The commission established the compartments and transfer rates of the ICRP model, taking into account previous research conducted by Leggett (1993), in order to accurately replicate the reported biokinetic patterns of lead. The fundamental characteristics of lead are as follows. Following the administration of radioactive lead through intravenous injection to adult individuals, it has been observed that around 55% of the total lead

activity is present in the blood, while the liver, skeleton, and kidneys contain approximately 15%, 10-15%, and 5% of the total lead activity, respectively, after a period of twenty-four hours. The majority of the remaining portion is linked to more soft tissue, with approximately 3-6% being eliminated within the initial 24-hour period.

Following the administration of an injection, it has been observed that over 99% of lead activity in the bloodstream becomes linked with red blood cells (RBCs). These RBCs then release lead back into the plasma, with a half-life of a few days. The elimination of lead from the liver and kidneys is shown to occur with apparent half-lives spanning many weeks. The first depletion of lead from red blood cells, liver, and other soft tissues during the early weeks can be attributed to a progressive excretion through urine and feces, accompanied by a concurrent accumulation in skeletal tissues (ICRP 1993).

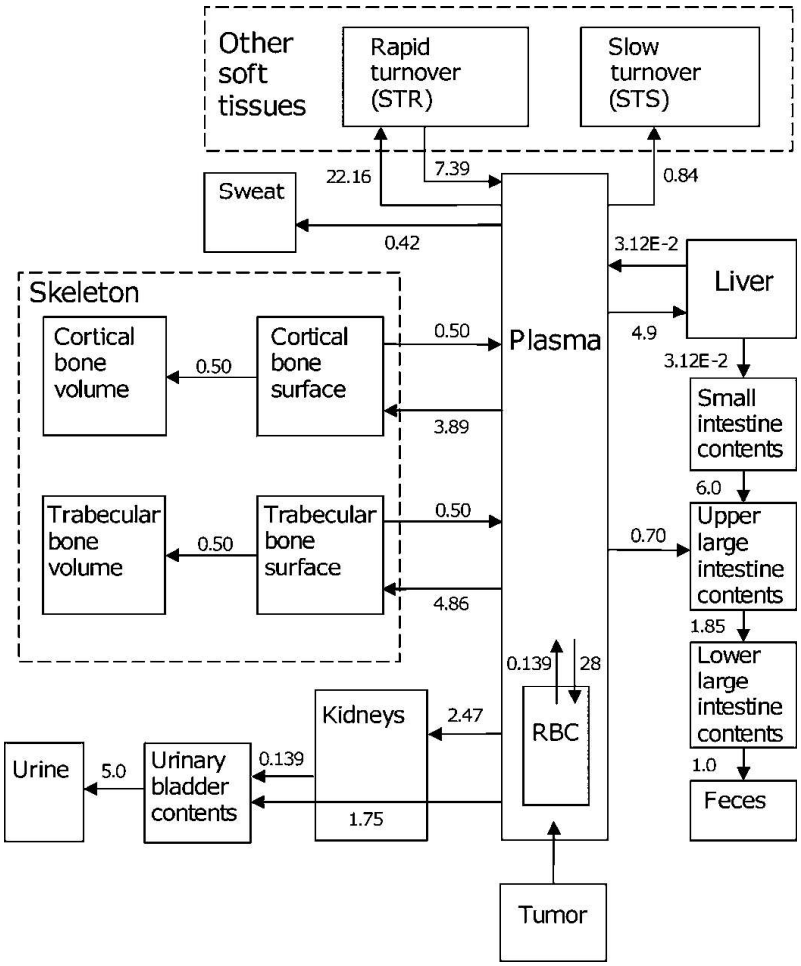

Figure 7 Compartimental biokinetic model of ^{224}-Ra

The delivery of dosage in DaRT is regulated by the half-life of ^{224}Ra, which is approximately 3.7 days. It is worth noting that 75% of the dose is delivered within the first week.

Consequently, some transfer rates incorporated in the ICRP model are of limited practical significance in this particular context. Consequently, a more streamlined iteration of the ICRP model for lead was implemented, wherein transfer routes with mean transfer times exceeding 40 days were excluded and certain compartments and transfer routes were consolidated. Figure 7 displays the amended International Commission on Radiological Protection (ICRP) model, along with the given values for all transfer rates, measured in days per unit. The primary components in this model encompass the circulatory system, skeletal structure, hepatic organ, renal organs, and additional non-osseous tissues. The blood compartment is partitioned into two distinct components, namely plasma and red blood cells (RBCs). The skeletal structure is partitioned into two distinct compartments: cortical and trabecular bone. Each compartment is further divided into sub-compartments based on surface and volume characteristics. The original ICRP model featured a distinction into exchangeable and non-exchangeable components, but this was omitted due to the relatively sluggish turnover rates associated with these components. The liver and kidneys are characterized as singular compartments, in contrast to the previous ICRP model that incorporated two sub-compartments for each of these organs. The expansive soft tissue compartment is partitioned into two distinct sub-compartments, characterized by varying rates of turnover. These sub-compartments are referred to as STR and STS, representing rapid and slow turnover rates, respectively. The model incorporates the transport of lead within the gastrointestinal (GI) tract, which is further subdivided into the small intestine, upper large intestine, and lower large intestine. The International Commission on Radiological Protection (ICRP) model delineates the process of lead excretion via urine, feces, and sweat. It is worth noting that the excretion of lead in hair and nails is considered to be of negligible significance for developmental and reproductive toxicity (DaRT) due to its sluggish rate. To mitigate the occurrence of impractical estimations about the dosage affecting the urinary bladder wall, the model incorporates the transfer of lead from the contents of the urinary bladder to urine. The application of the simplified version of the International Commission on Radiological Protection (ICRP) model to the Dosimetry and Risk Assessment Tool (DART) yielded findings that were within a 1% margin of agreement with the original ICRP model. Additionally, the simplified model's results were within around 10% of the original Leggett's model.

To accurately replicate the time dynamics of ^{212}Pb absorption in the various model compartments throughout a DaRT therapy, the tumor is depicted as an independent entity. The implanted ^{224}Ra sources deliver ^{212}Pb to the tumor, which then enters the bloodstream at a rate determined by the anticipated probability of ^{212}Pb leakage (Pleak (Pb)). This probability refers to the likelihood of a ^{212}Pb atom released from the source decaying outside of the tumor. Further details can be found in the appendix.

To maintain simplicity, we make the assumption that the chance of leakage, and thus the rate at which ^{212}Pb is cleared from the tumor, remains constant throughout time. It is also assumed that the isotope ^{212}Pb is released from the tumor into the bloodstream. The

model, which is extensively explained in the appendix, is executed by numerically solving a system of interconnected first-order linear ordinary differential equations with constant coefficients. These equations govern the transfer of lead between all compartments.

Due to the necessity of considering the potential redistribution of ^{212}Bi in relation to ^{212}Pb within the organism, a simultaneous solution is obtained for the biokinetic model of ^{212}Bi alongside that of ^{212}Pb.

The mathematical description of this model is provided in the appendix of ref [], and it is based on the assumptions outlined in ICRP Publication 67. Bismuth is eliminated from all tissues, except for bone volume, and is transferred to the plasma at a rate of 0.035 per day. When bismuth enters the plasma, it is distributed to various bodily compartments. Approximately 35% is excreted through urine, 7% is eliminated through the gastrointestinal system and subsequently excreted in feces, 35% is filtered by the kidneys, 5% is processed by the liver, and the remaining 18% is distributed to different tissues (more breakdown provided below). The plasma clearance rate is 50 d^{-1}.

The production of ^{212}Bi occurs through the process of ^{212}Pb decay within various compartments. Within the confines of the bone structure, it is postulated that the population of ^{212}Bi is primarily influenced by the decay processes of both ^{212}Pb and ^{212}Bi itself, without any involvement of exchange terms. Similar to the behavior observed in the case of ^{212}Pb, the egress of ^{212}Bi from the tumor is likewise attributed to its association with the plasma. To ensure simplicity in our analysis, we make the assumption that the average clearance time of ^{212}Bi from the tumor is equivalent to that of lead. It should be noted that based on preclinical data, it has been seen that ^{212}Bi is in a state of secular equilibrium with ^{212}Pb within the tumor. As a result, the average time it takes for bismuth to be cleared from the tumor can be considered significantly longer than the half-life of ^{212}Bi. Further details can be found in the appendix. The biokinetic model for ^{212}Bi incorporates the identical compartments seen in the simplified ICRP lead model, except for the merging of the two soft tissue compartments. Given that the ICRP model for bismuth does not explicitly address the transfer of bismuth from the kidneys to the urine bladder contents, this particular pathway is not incorporated in the model. Instead, the model assumes that ^{212}Bi directly reaches the urinary bladder contents from the plasma. The user's text is incomplete and does not provide enough information to be rewritten academically The assumption is made that the transfer rates between the segments of the gastrointestinal system are equivalent to those in the reference model.

The International Commission on Radiological Protection (ICRP) did not provide an analysis or resolution regarding the issue of bismuth transfer between the plasma and red blood cells (RBCs). Therefore, for the purposes of our analysis, we make the working assumption that the rate at which bismuth is transferred from red blood cells (RBCs) to the plasma is equivalent to that of lead, specifically 0.139 d^{-1} (which corresponds to a half-life of 5 days). The transfer of ^{212}Bi from the plasma to the red blood cells (RBCs) is hypothesized to be encompassed within the 18% fraction that is eliminated from the

plasma to all organs, excluding the urinary bladder, kidneys, liver, and gastrointestinal (GI) tract. The allocation of the 18% is distributed in the following manner: 8.4% is assigned to red blood cells with a transfer rate of 4.22 d^{-1}, 6.9% is allocated to soft tissue with a transfer rate of 3.46 d^{-1}, 1.5% is designated to the trabecular bone surface with a transfer rate of 0.73 d^{-1}, and 1.2% is assigned to the cortical bone surface with a transfer rate of 0.59 d^{-1}. The transfer rate ratios for these routes, which were not provided by the International Commission on Radiological Protection (ICRP), were assumed to be equivalent to those for lead for the sake of simplicity.

The assumption is made that the two ephemeral offspring of ^{212}Bi, namely ^{212}Po and ^{208}Tl, are in a state of secular equilibrium with their progenitor. Therefore, the cumulative activity in each organ for the corresponding substances are 0.64 and 0.36 times those of ^{212}Bi.

2.4.3 Allocation of activity to specific organ

With the exception of the liver and kidneys, the biokinetic model does not establish a connection with particular soft-tissue organs. To determine the dosage for all organs encompassed within the MIRD scheme, it is imperative to assign cumulated activity from the biokinetic model compartments to each specific organ. The allocation process involves the distribution of resources from the soft tissue compartment, which is determined by the organ mass and estimated total soft tissue mass, as well as from the blood, which is determined by the blood volume in each organ. The OLINDA/EXM computer code utilized organ masses sourced from Stabin and Siegel whereas blood volumes were obtained from ICRP Publication 89 (ICRP, 2002). The supplementary online material at stacks.iop.org/PMB/55/1203/mmedia contains Table S1, which provides a comprehensive list of organs for which the dose is estimated. The table includes information on the organs' masses, blood volumes (expressed as a percentage of the total blood volume), and, when relevant, their contents. The total body mass was recorded as 73.7 kg using the OLINDA/EXM software, whereas the total blood mass was estimated to be 5.6 kg based on the ICRP 2002 guidelines.

The researchers determined the overall mass of soft tissue, excluding the liver and kidneys, by subtracting the masses of these organs, the mass of the dry skeleton and teeth (5.2 kg), the total mass of blood (5.6 kg), and the masses of the stomach contents (0.26 kg), gastrointestinal tract contents (0.80 kg), and urinary bladder contents (0.21 kg) from the total body mass (73.7 kg). This calculation yielded a value of 59.4 kg for the mass of soft tissue. The equation (2):

$$A_{k,i} = \frac{M_i}{M_{ST}} A_{k,ST} + f_{BV,i} A_{k,blood} \qquad (2)$$

calculates the cumulated activity of the kth isotope, denoted as $A_{k,i}$in an organ of mass M_i (excluding the liver and kidneys). The calculation takes into account the mass of the organ, the cumulated activities in the soft tissue $A_{k,ST}$ and $A_{k,blood}$ blood compartments, and the blood volume in the ith organ $f_{BV,i}$. For the specific case of lead, the cumulated activity in the soft tissue $A_{Pb,ST}$ is calculated as the sum of $A_{Pb,STR}$ and $A_{Pb,STS}$. The term "blood" refers to the collective measure of accumulated activities within both the plasma and red blood cells (RBCs).

Several exceptions were handled in a distinct manner. According to ICRP Publication 89, the combined blood volume for the stomach and oesophagus is estimated to be 1%. The blood volume assigned to the stomach wall was determined by multiplying 1% with the mass of the stomach wall (158 g) and dividing it by the sum of the masses of the stomach wall and oesophagus (40 g), resulting in a value of 0.8%. ICRP Publication 89 presents the blood volume of the entire large intestine as a unified value of 2.2%, without distinguishing between its lower and upper segments, which are considered individually in the calculation of radiation dose.

The blood volumes of the walls of the upper and lower large intestine were determined based on their mass ratio, resulting in a value of 1.25% for the former and 0.95% for the latter. The lungs are subjected to specialized treatment as well. According to Stabin and Siegel (2003), the combined mass of the lungs, including the blood contained inside them, is said to be 1.0 kg. Approximately 0.5 kg of this total mass is attributed to the presence of pulmonary blood. To assign accumulated activity to the lungs, equation (1) utilized the net mass of lung tissue (0.5 kg) instead of 1 kg.

Within the anatomical divisions of the bone, the red bone marrow, which will be further examined later, is identified as the organ that limits the dosage (alongside the kidneys). It receives approximately 4% of the total blood volume, with a minor additional contribution from the soft tissue compartment based on its mass. However, in practice, it was determined that the contribution from the soft tissue compartment is insignificant compared to the dose originating from the blood. The cortical bone blood component, which was determined to be 0.8%, was allocated to the cortical bone volume compartment. This compartment represents the blood vessels present in the Haversian system. To ensure a cautious approach, the trabecular bone blood component of 1.2% was allocated to the compartment representing the surface of the trabecular bone.

The organs that lacked information regarding blood volume in ICRP Publication 89, namely the breasts, ovaries, uterus, thymus, and gall bladder wall, were allocated cumulated activities based on the blood fraction contained in small vessels. This fraction constitutes 56.5% of the total blood volume, as stated in the ICRP 2002 publication. The allocation was determined by considering the ratio between the masses of these organs and the total soft tissue mass, which encompasses the liver and kidneys.

2.4.4 Internal Dose assessment

The calculation of the dose to all organs involves initially establishing the values for all input parameters. The experiment involved the administration of ^{224}Ra activity to the tumor, followed by an assessment of the effective desorption probability of ^{212}Pb from the source. Additionally, the average leakage probability of ^{212}Pb from the tumor and the average clearance rate coefficient were determined.

The presence of ^{212}Bi originating from the tumor can be observed (refer to the appendix for precise definitions of all parameters). the given data, it may be concluded that the majority of participants preferred option A over option B.

The determination of cumulated activities of ^{212}Pb, ^{212}Bi, is accomplished through the utilization of biokinetic calculations.

The isotopes ^{212}Po and ^{208}Tl are distributed among all model compartments and subsequently allocated to various organs. The doses to all organs, including alpha, beta, and gamma doses, are subsequently determined using the MIRD technique. The alpha and beta doses presented in the following analysis were computed using a proprietary computer code and afterwards compared to the outcomes derived from the OLINDA/EXM 1.1 code. The calculation of gamma doses was exclusively performed using the OLINDA/EXM 1.1 software. In the case of conventional organs, the determination of alpha and beta doses involved the assumption that the complete energy of the alpha particle, or the average energy of the beta particle, is locally deposited during each decay event, also known as self-dose. In the case of hollow organs, the calculation of the dose to the wall involved the summation of the self-dose of the wall and the contribution originating from the contents of the organ.

The aforementioned value is determined, in accordance with the convention utilized in the MIRD scheme, as

$$D_{wall}(\text{wall} \leftarrow \text{contents}) = f_c \frac{\mathrm{A}_{contents} \times E}{2M_{contents}} \quad (3)$$

A value of fc = 0.01 was assigned to the gall bladder, stomach, small and large intestines for alpha particles. Conversely, a value of f_c = 1 was assumed for the heart and urine bladder wall, consistent with OLINDA/EXM 1.1 (Stabin, 2009). A value of fc = 1 was assigned to all hollow organs for beta particles (Stabin and Siegel, 2003).

The alpha-particle absorbed fractions for bone targets, specifically the red bone marrow (RM) and bone surface (BS), were obtained from the study conducted by Stabin and Siegel in 2003. These absorbed fractions were sourced from OLINDA/EXM 1.1, with two adjustments made. The absorbed proportion for alpha particles that are exposed to the

bone surface from the red marrow was assumed to be 0.09 for all energy levels, as stated in the work of Stabin and Siegel (2003). Additionally, the absorbed fractions for ^{212}Po were determined using linear extrapolation up to 8.79 MeV. It is worth noting that the absorbed fractions provided by OLINDA are limited to the range of 3-8 MeV. The absorbed fractions pertaining to beta particles were obtained from the study conducted by Stabin and Siegel in 2003. The alpha particle values utilized in this study are provided in table S2, which can be found in the supplementary online material accessible at stacks.iop.org/PMB/55/1203/mmedia.

2.4.5 Tolerance dose estimates

The effective range of application of DART, with regards to the maximum amount of ^{224}Ra activity that can be administered to the patient without causing harm, will be constrained by the necessity to avoid adverse non-stochastic tissue reactions (specifically, deterministic tissue injury such as kidney failure), which may manifest shortly after the treatment or within a few months or years7. To determine the acceptable level of ^{224}Ra activity, the organ doses that have been determined are integrated with two supplementary datasets: a compilation of tolerance doses for all organs and a corresponding compilation of relative biological effectiveness (RBE) values. The tolerance doses utilized in this study were derived from ICRP Publication 41, which was published by the International Commission on Radiological Protection in 1984 (ICRP, 1984). The aforementioned values are to the cumulative doses of gamma or x-ray radiation administered using conventionally fractionated external beam radiation therapy (EBRT), resulting in tissue damage in 1-5% of patients. Each organ is associated with a specific form of injury, which is elaborated upon in Table 2. The RBE estimates pertaining to deterministic effects were obtained from ICRP Publication 58, specifically ICRP 1989. The values utilized in the analysis are the ones that correspond to the limit of extremely small doses (RBE_m), as determined by the linear-quadratic model (ICRP 1989). It should be noted that the data presented in ICRP Publication 58 pertains to animal tests conducted in vitro and in vivo, specifically with heavy ion beams such as carbon, neon, and argon. These investigations were conducted on mice and hamsters.

In the context of this investigation, the RBE_m values used as references were derived from carbon ion beams with linear energy transfer (LET) ranging from 80 to 150 keV μm−1, specifically those administered at a spread Bragg peak of 4 cm. In instances where the organ in issue did not have access to RBE_m data, a range of 2-5 was utilized. This range was chosen based on the observed range of RBE_m values for deterministic effects caused by heavy ions.

The estimation of the alpha-particle tolerance dose for each organ was conducted by dividing the tolerance dose for that organ in x-ray radiation by the corresponding value of relative biological effectiveness (RBE_m).

Chapter 3 The application of DaRT in patients

Published in: International Journal of Radiation Oncology, Biology, Physics

Popovtzer A, Rosenfeld E, Mizrachi A, Feliciani G, et al

Initial Safety and Tumor Control Results From a "First-in-Human" Multicenter Prospective Trial Evaluating a Novel Alpha-Emitting Radionuclide for the Treatment of Locally Advanced Recurrent Squamous Cell Carcinomas of the Skin and Head and Neck.
https://doi.org/10.1016/j.ijrobp.2019.10.048

The experimental studies described above represent the starting point for the applicability of DaRT treatment on patients. Indeed it was demonstrated that atoms released from ^{224}-Ra migrate to considerable distances from the source giving rise to a substantial dose over a region measuring several millimiters. This scientific evidence can be translated after the proper pre-clinical studies of efficacy on mice for the treatment of cutaneous squamous cell skin carcinoma (cSCC) in humans. Indeed as an institution (IRST) we participated into the "first in human" clinical trial N. CTP-SCC-00 (NCT03015883) with the objective to assess safety and effectiveness of DaRT technique. Hereby we report an extrapolation of the co-authored paper and published in the international journal of Radiation Oncology, Biology, Physics by Popovtzer et al. Based on a number of preclinical studies that have shown the efficacy of DaRT in eradicating cancer cells in vitro and inducing tumor responses in vivo [18, 22], we commenced a feasibility study in 2017 to assess the viability of utilizing this innovative method for treating patients diagnosed with squamous cell carcinomas (SCC) affecting the skin and head and neck regions. This thesis provides a comprehensive description of the feasibility, safety profile, and first tumor control outcomes observed in the inaugural clinical trial involving human subjects.

3.1 Patient Enrollment

The study included the enrollment of patients with SCC lesions from February 2017 to March 2019. These patients were recruited from two medical centers: Rabin Medical Center Petach in Tikva, Israel and the Instituto Scientifico Romagnolo for Lo Studio e la Cura dei Tumori in Meldola, Italy. Both medical institutes obtained clearance from their respective institutional ethical committees as well as the local ministries of health. Prior to commencing protocol therapy, informed consent was obtained from all patients.

The main aim of this study was to function as a preliminary investigation and assess the safety of the Ra-^{224} DaRT seed treatment. This involved examining the occurrence, intensity, and frequency of negative events, as classified by the Common Terminology Criteria for Adverse Events (version 4.03).

The study's secondary aims encompassed the assessment of early tumor responses to the Ra-^{224} DaRT seed treatment using clinical and imaging evaluations conducted 30 to 45 days after DaRT insertion. Additionally, a preliminary evaluation of local progression-free survival (PFS) was conducted.

The eligibility criteria encompassed all individuals who had received a biopsy confirming the presence of squamous cell carcinoma (SCC) on the skin, as well as the head and neck region. A majority of the patients (60.7%) in the study had recurrent and previously treated disease, which had been managed with surgical intervention, prior external beam radiation therapy (RT), or a combination of both modalities. Specifically, 13 out of 31 patients (42%) had undergone previous RT. The remaining proportion of individuals (39.3%) exhibited a primary tumor. In addition to the existing criteria, the study required tumors to have a maximum size of less than 5 centimeters in the longest diameter and to be free from nodal dissemination. Inclusion criteria for this study required patients to be at least 18 years of age, possess an Eastern Cooperative Oncology Group (ECOG) Performance Status Scale score of less than 2, and have a life expectancy exceeding 6 months.

Three individuals exhibited significant protocol deviations. In one participant, immunosuppressant drugs were administered due to a prior kidney transplant, despite this being a violation of the exclusion criteria. In a separate instance, a patient experienced a parasite infection that occurred during the presence of the DaRT implant, resulting in the need for its early removal 10 days after its initial installation. An additional patient was deemed unevaluable due to her unfortunate demise resulting from pneumonia unrelated to the DaRT surgery. The manifestation of this pneumonia occurred clinically three weeks after the aforementioned procedure. Although the aforementioned patients were included in the examination of toxicity, their tumor response could not be evaluated. Consequently, these individuals are excluded from all statistical analyses pertaining to response and outcome. Consequently, this study presents an examination of toxicity and baseline values for all lesions that underwent treatment (31 lesions in 28 patients, Table 1). Twenty-eight lesions in 25 patients were evaluable for response at 30 to 45 days postinsertion and they are reported in the response analysis.

Table 1 Patient and disease characteristics

Age (years)		Number of patients	28
		Mean (standard deviation)	78.7 ± 11.2
		Median (range)	80.5 (59, 94)
Sex	Male	% (n/N)	71% (20/28)
	Female	% (n/N)	29% (8/28)
1.1.1	1.1.2	1.1.3	1.1.4
1.1.5	1.1.6	1.1.7	1.1.8
Tumor volume (cm^3)		Number of lesions	31
		Mean (±standard deviation)	3.9 (±6.4)
		Median (range)	1.7 (0.2, 33.9)
Primary versus recurrent	Primary	% (n/N)	35.5% (11/31)
	Recurrent	% (n/N)	64.5% (20/31)
Tumor location	Nonhead and neck	% (n/N)	13% (4/31)
	Head and neck	% (n/N)	87% (27/31)
Previous RT	Yes	% (n/N)	42% (13/31)
	No	% (n/N)	58% (18/31)
Previous surgery	Yes	% (n/N)	61.3% (19/31)
	No	% (n/N)	38.7% (12/31)

Abbreviation: RT = radiation therapy.

3.2 Study Design

In the initial phase of the study, a total of four patients were recruited with the objective of assessing the feasibility of tumor implantation. Feasibility, in this context, was defined as the successful implantation of the tumor without any occurrence of grade 3 toxicity during a three-month period. After confirming the feasibility, an additional 24 patients were recruited to conduct a more comprehensive assessment of toxicity and initial efficacy. Participants were screened according to the specified eligibility criteria outlined in the protocol, and they were included in the study after providing written informed permission. Demographic information and concomitant drugs were collected during the screening session. The first step was conducting a CT simulation, followed by the delineation of the clinical tumor volume. This was done by considering clinical examination findings and evaluating baseline CT or magnetic resonance imaging scans.

The planned target volume (PTV) was established by extending the clinical tumor volume (CTV) by 5 millimeters, utilizing a geometric loading pattern and technology. To ensure proper dosimetric coverage, the Alpha DaRT was positioned using strands spaced at 5-mm intervals and seeds inserted 5 mm beyond the tumor boundary. In cases where the size of the tumors exceeded 5 mm in depth, the utilization of bior multiplanar needle geometry was implemented. The treatment procedure involved the administration of radioactive seeds, each carrying 2 mCi of ^{224}Ra, which were put into the tumor site under local anaesthetic. This procedure was conducted in an outpatient environment.

In contrast to gamma and beta sources, where the dose at any given place is dictated solely by the geometric arrangement of the source, the dose from DaRT sources is influenced by both the geometric position and the diffusion properties of the alpha emitters within the tumor. Nevertheless, a preclinical investigation including the implantation of SCC tumors in mice yielded valuable quantitative data pertaining to

diffusion characteristics and the necessary dosage for the eradication of tumor cells.The user's text is already academic. A direct comparison was conducted between the observed distribution of radioactive atoms, which allowed for the measurement of dose and dose rate, and the region of cell death observed in the tumor. A minimum cumulative dose of around 10 gray was necessary, resulting in a death area with a diameter of 5 mm surrounding the source. The formulation of the treatment plan was predicated upon the preclinical findings. The DaRT seeds were inserted in accordance with a pre-established plan, taking into consideration the precise quantity of applicators and DaRT seeds per applicator. Following the implantation of the DaRT seeds, a routine post-procedure brachytherapy computed tomography (CT) scan was performed in order to evaluate the final positioning of the seeds within the tumor for the purpose of quality assurance (QA) assessment. The quality assurance assessment provided evidence that the tumor volume was consistently covered by DaRT seeds, with a level of coverage of 95%. If the presence of undercoverage was identified through the use of a quality assurance check (where n is a multiple of 3), more seeds were included prior to the completion of the implantation process.

The DaRT seeds were surgically placed at a precise distance of 10 mm away from significant blood vessels, such as the carotid artery. Radiation is a phenomenon characterized by the emission of energy in the form of electromagnetic waves or particles. Geiger monitor with a collimator was used to check emission of radioactivity from the seeds immediately after insertion. Seeds were removed 15 to 30 days after implantation with or without local anesthesia, depending on the anatomic location of the implanted site.

3.3 Radionuclide and applicators

The administration of the DaRT seeds was conducted utilizing an applicator manufactured by Alpha Tau Medical, Limited, a company based in Tel Aviv, Israel.

Each seed is comprised of a hollow wire made of 316LVM stainless steel, measuring 10 mm in length and 0.7 mm in diameter. The surface of the wire is coated with radium-^{224}. The seeds were arranged in a linear fashion and attached to a single monofilament suture. The seeds are enclosed within the applicator needle and coated with glycerin. Each applicator has the capacity to accommodate 1 to 6 seeds.

The DaRT applicator comprises two primary components that are typically found in interstitial brachytherapy applicators. These components include a needle, along with an attached hub, which is utilized for the percutaneous placement of the DaRT into the tumor. Additionally, a stylet, also with an attached hub, is employed to deploy the DaRT encapsulated seed(s) at the designated position within the tumor (Figure 8).

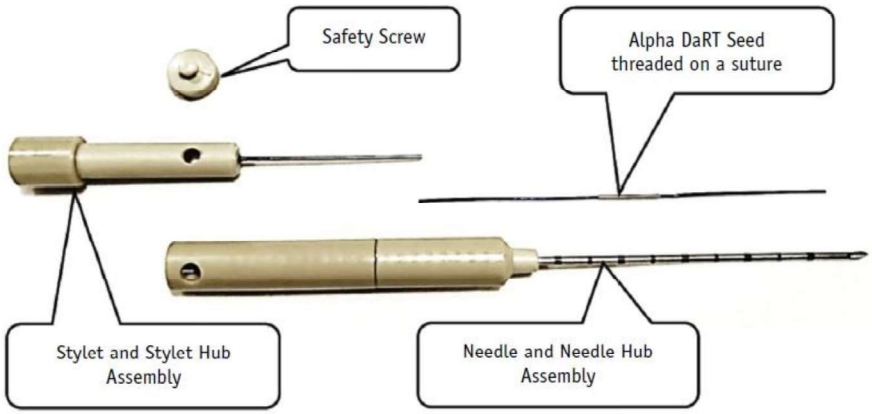

Figure 8 DaRT applicator schematics

Furthermore, the device, consisting of an applicator and seeds, is equipped with a protective cap that remains in place over the needle's tip to safeguard it from potential harm. Additionally, a safety pin is included to prevent unintended detachment of both the needle and stylet. The Alpha DaRT device is composed of DaRT seeds that are housed within the DaRT applicator.

3.4 Follow up

The study's follow-up examinations consisted of doing repeated blood tests and urinalysis, as well as additional measures of blood and urine radiation levels. Additionally, the researchers assessed the ECOG Performance Status scale at specific time points, namely 4, 9, and 30 days after the insertion of DaRT. All modifications to concurrent drugs were documented throughout the duration of the trial. Adverse occurrences were evaluated during every study visit and documented on case report forms. The measurement of tumor size was repeated between 30 and 45 days following the insertion of Ra-^{224} DaRT seeds. The determination of changes in tumor size was established using physical examination, and in the majority of instances, imaging techniques such as positron emission tomography-CT scans or CT scans were further employed to evaluate the response.

The evaluation of tumor response was conducted during a follow-up visit occurring between 30 and 45 days after treatment initiation. The Response Evaluation Criteria in Solid Tumors (version 1.1) were employed for this assessment. The sole focal area affected by radiation, namely the tumor, was exclusively regarded as the target lesion for the purpose of evaluating its response. In this study, it was observed that 28 out of the total 31 lesions were considered evaluable for response, as previously mentioned in the section pertaining to patient enrollment.

The criteria for evaluating the response to treatment were established as follows: a complete response (CR) was defined as the complete disappearance of the irradiated

tumor; a partial response (PR) was defined as a decrease of at least 30% in the longest dimension of the irradiated tumor; progressive disease was defined as an increase of at least 20% in the longest dimension of the irradiated tumor, with reference to the smallest longest dimension recorded since the initiation of radiotherapy; stable disease was defined as neither sufficient shrinkage to meet the criteria for a partial response nor sufficient increase to meet the criteria for progressive disease, with reference to the smallest sum since the start of treatment.

A biopsy was performed (n=5) between four to six weeks after the insertion of Ra-^{224} DaRT seeds, in cases where there was clinical suspicion of residual disease. Surgical intervention or systemic therapy was administered in instances where residual illness was histopathologically proven. The patients were then assessed at two-month intervals to ensure ongoing follow-up observation.

3.5 Statistical Analysis

The statistical analyses were conducted using SAS version 9.4, developed by SAS Institute in Cary, North Carolina. The study findings were analyzed, and quantitative data were described using descriptive statistics such as mean, standard deviation, minimum, median, and maximum values. Categorical variables were reported as counts and percentages. The incidence rates of serious adverse events (SAEs) are reported alongside 95% score confidence intervals (CI) in a two-sided manner. The Kaplan-Meier method was utilized to produce estimates for the probability of overall survival and local progression-free survival. A log-rank test was employed to compare the survival curves of two groups. The measurement of overall survival was conducted starting from the date of the DaRT insertion surgery. The local PFS was stratified according to the recorded date of the initial response. The duration of follow-up for the study participants ranged from 1.45 to 23.36 months, with a median follow-up time of 6.7 months.

3.6 Results

This study assessed a total of 31 lesions in 28 patients throughout the period from February 2017 to March 2019. The patient sample consisted of 22 individuals from Rabin Medical Center Petach, Israel, and 6 individuals from Instituto Scientifico Romagnolo for Lo Studio e la Cura dei Tumori, Italy. Out of the total sample size of 28 patients, it was seen that 3 individuals underwent treatment on two occasions, each for the purpose of addressing distinct malignancies. Consequently, the cumulative number of lesions identified across the entire cohort amounted to 31. The demographic information, clinical features, and tumor location of the 28 patients who underwent treatment are presented in Table 1. The specific locations that were treated in this study comprised the skin (n =

12, with 4 of them located in the extremities), ear (n = 7), lip (n = 5), tongue (n = 3), nose (n = 2), and parotid (n = 2). All observed lesions were classified as squamous cell carcinoma (SCC). The mean quantity of Ra-^{224} DaRT seeds that were implanted into the tumors was 27.72 seeds, with a range of 3 to 169 seeds. The average duration of the treatment was 16.3 ± 4.3 days. The mean activity of the seeds on the day of insertion was recorded as 55.42 to 61.46 mCi.

3.7 Biosafety evaluation

Measurements of radioactivity were taken at the site of insertion, as well as at other regions of the body, and in samples of blood and urine. Additionally, the patients' vital signs and overall medical condition were assessed and recorded both at the beginning of the study and during follow-up visits. In the population of individuals who had the aforementioned procedure, the mean levels of radioactivity in the blood and urine were found to be around 41.2 ± 34.4 kBq/L and 6.1 ± 5.3 kBq/L, respectively, at roughly 4 days post-treatment.

The mean levels of radioactivity in the blood and urine exhibited a decline, reaching values of 12.7 ± 10.2 kBq/L and 2.5 ± 2.9 kBq/L, respectively, roughly 9 days following the administration of treatment. There was an absence of detectable levels of radioactivity in the blood and urine 30 days following treatment, with the exception of one patient who received DaRT seeds for two separate squamous cell carcinoma (SCC) lesions in two distinct sessions, spaced 15 days apart. Due to the proximity of these sessions, radioactivity remained detectable at day 30 after the initial insertion procedure. On the thirtieth day following the second treatment, the patient exhibited an absence of detectable levels of radioactivity in both their blood and urine samples.

The alpha doses to the lungs, kidneys, and bone marrow resulting from the radioactive decay product of DaRT (^{212}Pb) were estimated by employing the model outlined by Arazi et al. These estimates were derived based on the analysis of blood and urine radioactivity measurements.The number 5. The likelihood of Pb-^{212} leakage, which represents the fraction of ^{212}Pb exiting the tumor through the bloodstream, was determined to be 0.40 ± 0.15 (40%). The mean and standard deviation of alpha dosage levels to the lungs, kidneys, and bone marrow were found to be 0.03 ± 0.02 cGy, 0.028 ± 0.017 cGy, and 0.012 ± 0.007 cGy, respectively. The aforementioned values fall within the acceptable range of radiation doses for the lungs, kidneys, and bone marrow, which are 1500, 500, and 100 cGy, respectively.

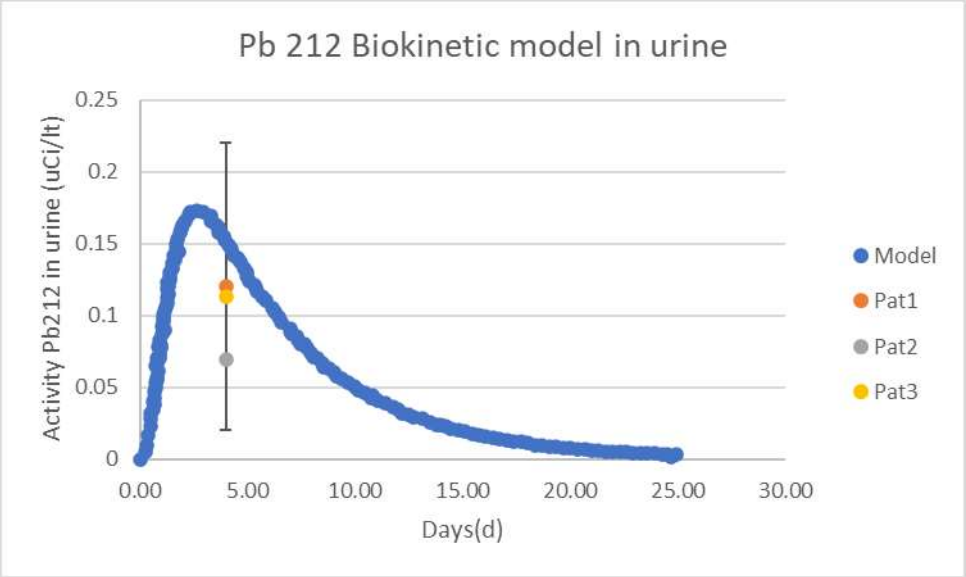

Figure 9 Biokinetic model for Pb ^{212} activity in urine

In Figure 9 the blue line represent the prediction of the bio-kinetic model calculations described above. The figure shows the overall excreted activity of pb-^{212} in the urine for a tumor treated with 75 microcuries of ^{224}Ra assuming 55% desorption probability and 20% leakage probability in function of time from treatment. Afterwards we superimposed the results of activity evaluation performed at our center on a HPGe spectrometer for 3 patients 4 days after treatments and normalizing the activity to the 75 uCi of the model. In general the model overestimated the measured concentration in urine however a very high uncertainty is associated with the measurement. In the figure we employed as error bars the standard deviation of measurements normalized to the 75 uCi of activity performed on all the 28 patients treated with DaRT.

3.8 Toxicity

Table 2 presents a summary of the occurrence of acute toxicity events that were detected within a period of up to three months following the insertion procedure of DaRT. The acute toxicity observed in patients undergoing Ra-^{224} DaRT seed treatment, which is believed to be potentially or highly associated with the protocol therapy, primarily manifested as localized pain (n=11) and erythema (n=10) at the site of implantation. This was followed by swelling (n=8) and mild skin ulceration (n=4). A significant proportion of patients, around 90%, experienced complete remission of pain and grade 2 skin ulcerations within a period of 3 to 5 weeks. Typically, the acute toxicities seen were successfully cured after a median duration of 15 days, with a range spanning from 4 to 183 days. In a sample of eight patients, the DaRT seeds were placed in close proximity

(within a distance of less than 5 mm) to bone and teeth. Notably, none of the patients experienced the development of osteoradionecrosis. Two serious adverse events (SAEs) were documented, and it was concluded that neither of them were associated with the protocol therapy. A patient in this study acquired pneumonia following therapy and later died due to their pre-existing poor performance status and other comorbidities. Cerebral edema in a second patient who underwent DaRT treatment for a squamous cell carcinoma (SCC) localized to the nose was determined to be caused by a previous radiation therapy (RT) administered to the base of the skull and posterior orbit. There were no device-related serious adverse events (SAEs) detected throughout the duration of the treatment or subsequent monitoring period. The study observed a device-related serious adverse event (SAE) incidence rate of 0% during the course of the study period, with a 95% confidence interval (CI) ranging from 0% to 12.06%. Additionally, the incidence rate of unrelated SAEs was found to be 7.14%, with a 95% CI ranging from 1.98% to 22.65%. As of the present time, there have been no instances of late toxicities observed.

Table 2 Incidence of acute local toxicity (n=31)

Acute local toxicity						
Severity grade		**1**		**2**		**3**
	Incidence	(%)	Incidence	(%)	Incidence	(%)
Erythema	11	-35%	9	-29%	0	0%
Swelling	6	-19%	8	-26%	0	0%
Pain	9	-29%	11	-35%	0	0%
Discharge	2	-6%	6	-19%	0	0%
Ulcer	4	-13%	3	-10%	0	0%
Paresthesia	3	-10%	0	0%	0	0%
Pruritus	3	-10%	0	0%	0	0%
Scarring	0	0%	1	-3%	0	0%

3.9 Initial tumor response

Out of the total of 28 individuals who had treatment, 28 out of the 31 treated lesions were assessed in order to ascertain the response of the tumors. The scope of this evaluation was restricted to patients who satisfied the predetermined criteria for participation in the study, adhered to the prescribed DaRT therapy protocol, and fulfilled the requirement of a minimum 6-week follow-up period after treatment.

The complete response (CR) rate to the ^{224}Ra DaRT seed treatment was observed in 22 lesions, accounting for 78.6% of the cases. Additionally, partial response (PR) was observed in 6 lesions, representing 21.4% of the cases, with tumor reduction ranging from 30% to 100%. Hence, it can be observed that every patient shown a certain degree of response to the administered medication. An exemplification of a comprehensive response is depicted in Figure 10. In the group of patients who did not undergo prior radiation therapy (RT), a total of 15 out of 16 patients (94%) exhibited a complete response (CR). Conversely, within the subgroup of patients who had received RT in the past, 7 out of 12 patients (58%) achieved a CR.

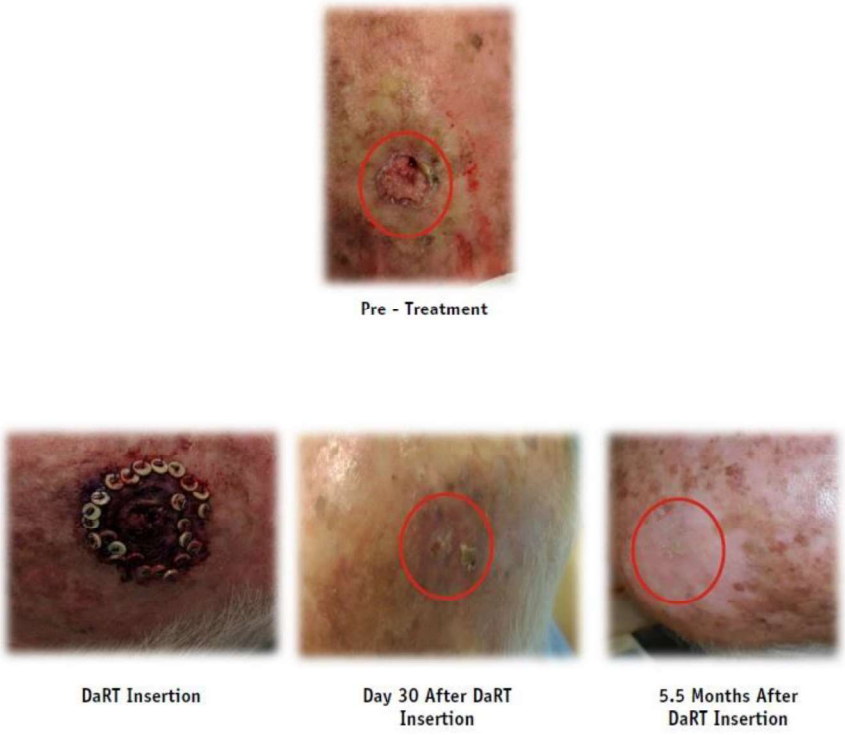

Figure 10 Deeply infiltrating SCC of the scalp with complete response noted at day 30.

Out of the 22 lesions that attained a complete response (CR), a total of 5 lesions experienced a local relapse specifically at the location where the DaRT implantation took place. This relapse occurred at a median time of 4.9 months, with a range of 2.43 to 5.52 months, following the treatment. The local progression-free survival (PFS) rate for all

patients at the one-year mark was assessed using the Kaplan-Meier method to be 44% (95% confidence interval [CI], 20.3-64.3%). The study found that among patients who initially achieved complete remission (CR) after treatment, the projected local progression-free survival (PFS) rate after one year, as determined by the Kaplan-Meier method, was 60%. A only 32% of the patients underwent a comprehensive one-year follow-up. Patients who had an initial complete response (CR) demonstrated considerably greater rates of local progression-free survival (PFS) and overall survival (OS) at the one-year mark, in comparison to those who acquired a partial response (PR). Specifically, the rates were 60.1% and 93% for CR patients, while PR patients had rates of 0% for both local PFS and OS (refer to Figure 11).

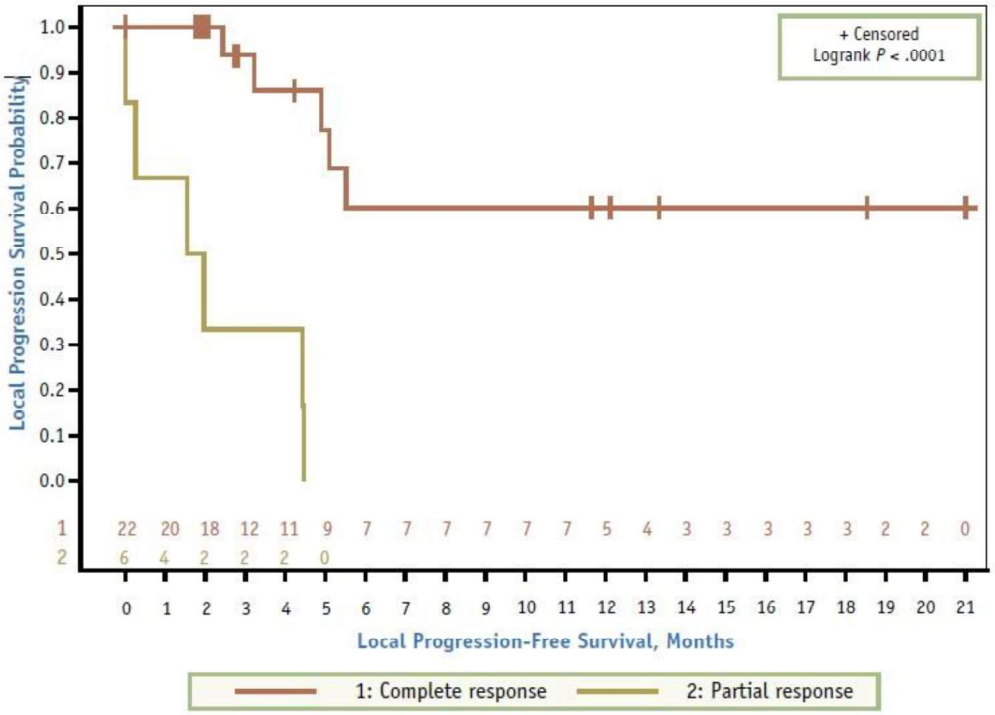

Figure 11 Patients' PFS kaplan meyer survival curve

The study found that the overall survival rates at 12 months after the implantation of DaRT were 75% (95% CI, 46.14-89.99%) for all patients and 93% (95% CI, 59.08-98.96%) for those who were classified as complete responders.

The duration of follow-up for the study participants ranged from 1.45 to 23.36 months, with a median of 6.7 months.

A singular patient, who underwent two separate treatments for skin squamous cell carcinoma (SCC), displayed a distinctive reaction. On both occasions, the treatment of one lesion resulted in an unexpected response, with a second unrelated lesion also exhibiting a complete response (CR) to the treatment.

At the one-year mark, there was no statistically significant distinction observed in the local progression-free survival (PFS) between primary lesions (those that were newly identified) and recurrent lesions (those that had reappeared) (P = 0.9). The median local progression-free survival (PFS) duration for patients with recurrent tumors was seen to be 5.5 months, while for those with initial tumors, it was recorded as 5.09 months. There was no statistically significant difference observed in the local progression-free survival (PFS) between recurring or primary lesions (P = 0.59) as well. There was no statistically significant difference observed in the first response rates and toxicity outcomes between individuals who had received prior radiation therapy (n = 12) and those who had not (n = 16) (p = .59). The median local progression-free survival (PFS) for patients who had received prior radiation therapy was found to be 5.2 months, while for those without a history of radiation therapy, the median local PFS was 5.1 months.

3.9 Discussion

In this article, we provide the initial findings from a clinical trial conducted on human subjects. The trial aimed to assess the feasibility and safety of using an alpha-emitting brachytherapy source for the treatment of locally progressed and recurring squamous cell carcinomas (SCCs) affecting the head and neck region. The primary objectives of the study were to evaluate the early toxicity associated with the treatment and to assess the tumor response. Given that the main objective of this research was to assess the feasibility, the population under investigation exhibited heterogeneity, with varying locations of treatment including the head, neck, and skin. The cohort included a group of patients who were deemed to have a high risk prognosis, consisting primarily of elderly individuals who were not suitable candidates for surgery (with a median age of 80.5). Moreover, a significant proportion of the participants in this study had received surgical intervention or had undergone prior chemotherapy and radiation therapy. Based on the first assessment conducted by the head and neck surgeon for all patients, it was concluded that opting for additional surgery instead of the DART brachytherapy treatment would likely result in a higher likelihood of experiencing negative health outcomes.

Despite the participants in this study having undergone extensive pretreatment, the observed toxicity thus far has been rather little. Specifically, 48% of patients experienced acute grade 2 toxicity, whereas no patients exhibited grade 3 or greater toxicity. Moreover, in all instances, the toxicity was cured within a span of one month.

The positive tolerance outcomes may be attributed to the highly precise dosage distribution achieved through the utilization of the DaRT technique. The proposed

methodology utilizes the decay process of radium-^{224}, resulting in the production of radon-^{220}, which has a short lifespan. The daughter atoms of radon-^{220} disperse inside the tumor microenvironment, generating a concentrated dosage cloud that exhibits limited diffusion beyond a 5 mm radius [8]. This innovative approach demonstrates significant potential. By employing precise seed placement geometry, it is possible to attain a highly accurate dose distribution, hence minimizing the potential radiation exposure to adjacent tissues. While the results revealed in our study are promising, it is imperative to conduct a more extensive follow-up in order to validate these findings.

The paper also emphasizes the noteworthy initial tumor responses reported in spite of the recurring and somewhat radioresistant malignancies that were prevalent among this group of patients. The reduction in tumor size following the installation of DaRT was shown to be significantly rapid, with noticeable changes generally occurring within the initial two weeks after the procedure. Furthermore, it has been observed that the response to this treatment has been long-lasting in the majority of instances.

The initial local response, with a 60% likelihood of complete remission of disease, appears to be more favorable when compared to previously reported outcomes of routine reirradiation utilizing external beam or traditional brachytherapy techniques, where the response rates are below 40% [23, 24]. CRs were noted in 58% of patients with radio-recurrence and in 94% of those who never previously received RT. The observed results can be partially explained by the improved radiobiological characteristics linked to alpha particle therapy. This form of treatment has the capacity to overcome radio-resistant clones and achieve higher effectiveness when compared to conventional brachytherapy gamma sources.
The present work serves as a noteworthy illustration of the successful replication and verification of preclinical investigations that shown remarkable tumor responses.The innovative development of a brachytherapy dose delivery that takes advantage of short-range diffusion of alpha particles is unique and could potentially be paradigm changing [22, 25–28].

Chapter 4 A case report of a possible abscopal effect

Published in: Journal of Contemporary Brachytherapy,

Clinical evidence of abscopal effect in cutaneous squamous cell carcinoma treated with diffusing alpha emitters radiation therapy: a case report.
Bellia SSR, Feliciani G, Del Duca M, et al,

4.1 Introduction about abscopal effect

The abscopal effect (AE) is a sporadic event of tumor regression following radiotherapy treatment observed at distance from irradiated site. For the first time, the term 'abscopal effect' was used by Mole in 1953 [29]. The word 'abscopal' comes from Latin 'ab' and 'scopos', which means 'position away from the target'. This effect is a rare clinical event, however, there have been reports of this effect in various type of cancers, not only in solid tumors. but also in leukemias and lymphomas [30–32]. In particular, for skin tumors, there have been reports of a case of Merkel cell carcinoma and several cases of melanoma [33–38]. Recently, there has been growing evidence that high linear energy transfer (LET) radiations, such as alpha particles, are more prone to leverage this effect rather than low-LET X-rays usually used in external beam radiation therapy (EBRT)[39, 40]. We report a case o fa patient affected by cutaneous squamous cell carcinoma (cSCC). This patient had multiple synchronous lesions and after the treatment of one of the lesion with diffusing alpha emitters radiotherapy (DaRT), an abscopal effect was observed on two distant lesions. As skin cancer incidence is rising worldwide and the interest in brachytherapy applications is growing continuously [41–43], we decided to propose this treatment as an alternative to surgery. Patient refused surgery, since it was already applied multiple times. Furthermore, we didn't consider external beam radiotherapy; in our opinion, expected toxicity and duration of the treatment would have been higher [44, 45].

4.2 Patient description

We report a clinical case with a 65-year-old female patient of Caucasian ethnicity who came with several synchronous epithelial lesions on the skin of her lower limbs. The individual resided in the Caribbean for a period of three years, specifically between the ages of 24 and 26. It is quite likely that she experienced excessive exposure to ultraviolet (UV) radiation during this time. Upon reaching the age of 58, the individual experienced the emergence of several metachronous epithelial cutaneous lesions, which were

subsequently treated through surgical excision. The majority of the observed cases were classified as cutaneous squamous cell carcinomas (cSCC), while a minority were identified as keratoacanthomas (KA) through the process of biopsy confirmation. There was an absence of any notable comorbidity in her medical history.

The patient reported that there was no spontaneous remission of any specific lesion. The clinical suspicion of multiple cutaneous squamous cell carcinomas (cSCC) was subsequently verified by the anatomo-pathological team upon evaluation of the most significant lesions, referred to as A and B (Figure 12). Lesion A seen in Figure 12 has a keratinizing erythematous nodule of around 15 mm. Conversely, lesion B shares similar characteristics but is bigger in size, measuring 18 mm, and displays an exophytic growth pattern. Lesion A was classified as G1, while lesion B was classified as G2.

As a therapeutic intervention, we have suggested the participation in the international 'first in man' clinical study N.CTP-SCC-00 (NCT03015883), which aims to evaluate the safety and efficacy of the DaRT technology [46]. The methodology employed in this study encompasses the utilization of the conventional interstitial brachytherapy technique, which capitalizes on the high relative biological effectiveness (RBE) of alpha particles.

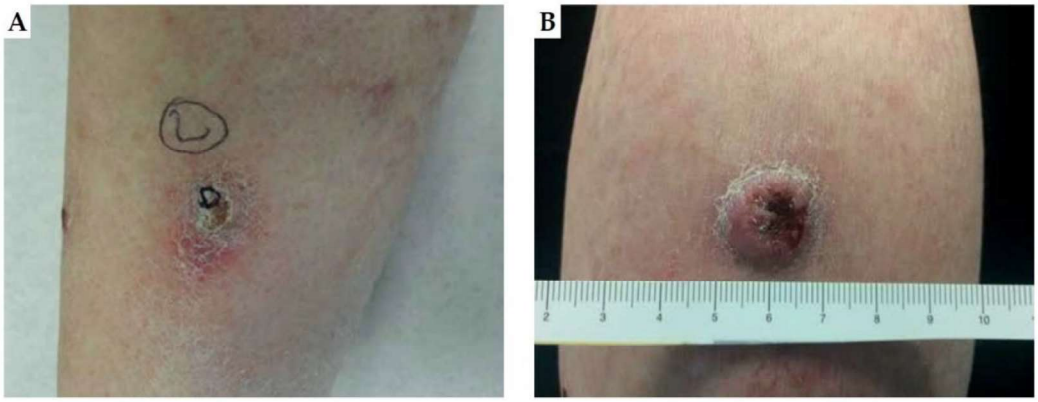

Figure 12 Lesion A (A) characterized by a keratinizing erythematous nodule of about 15 mm and lesion B (B) that is slightly larger (18 mm), with the same characteristics and exophytic

The lesions were captured using digital photography and subsequently measured using a physical ruler before the injection of DaRT seeds. The imaging procedure was conducted utilizing a SIEMENS Biograph MCT 20 flow 4R PET/CT scanner, following a normal PET/CT clinical protocol. The patient adhered to a minimum fasting period of 6 hours before to the intravenous administration of 18F-FDG at a dosage of 3.7 MBq/kg. The concentrations of serum glucose were assessed prior to the injection of FDG and were found to be below 200 mg/dl.

Following the PET/CT scan imaging, the task of delineating the gross tumor volume (GTV) was undertaken by a professional in the field of radiotherapy. The clinical target volume (CTV) is derived from the gross target volume (GTV) through the use of an isotropic extension of 5 mm. This expansion is necessary to encompass microscopic subclinical illness specific to this particular histological type. Baseline lesion extension is determined by measuring physical and radiological parameters. In subsequent interventions involving varying histology and tumor sizes, it is possible to consider alternative margins based on the radiation recommendations for non-melanoma skin cancer [47].

4.3 Treatment planning procedure

We remind DaRT technique description to Chapter 2 and 3.3 and we focus here on the treatment planning procedure.

A treatment plan was established using PET/CT images in order to determine the optimal number of seeds required to fully include the clinical target volume (CTV) throughout the intervention. The Oncentra brachytherapy treatment planning system was utilized to accurately organize the necessary quantity of seeds and to evaluate the potential entry places of needles. The treatment planning procedure is depicted in Figure 13A.

The seeds, each containing 100 kBq of ^{224}Ra, were positioned in accordance with the geometric arrangement of the Paris system, which was modified to accommodate the varying sizes of DaRT seeds. These sizes ranged from 1 cm to 6 cm, and were compared to linear sources. The interspacing is adjusted based on the Paris system, with an ideal interspacing ranging from 14 mm to 5 mm, as a result of the alpha emission characteristics of the ^{224}Ra source. The computation of precise dosage for alpha particles is not possible using a commercially available Treatment Planning System (TPS) due to the absence of dose deposition evaluation. However, according to the information provided in reference [20], it is assured that a dosage of 10 Gy will be achieved at a radial distance of 2.5 mm. Moreover, based on our empirical observations, it is beneficial to do a geometric assessment before to the interventional procedure, ensuring an accurate estimate of the lesion's depth. When the depth of the lesion exceeds 5 mm, it becomes imperative to provide the treatment using multiple planes. Consequently, we conducted an estimation involving the utilization of 5 needle applicators, each containing 2 seeds for the treatment of lesion A, which possesses a diameter of 15 mm and a depth of 4.5 mm. In total, 10 seeds were employed for this purpose. Additionally, for the treatment of lesion B, which has a diameter of 18 mm and a depth of 6.5 mm, we utilized 5 needle applicators loaded with 2 seeds and 4 needle applicators loaded with 1 seed, resulting in a total of 14 seeds being employed.

The treated lesion B that has grown from treatment planning session; B) The pretreatment planning session, 5 needles of 2 seeds spaced between each other of about 3-4 mm to account for lesion swelling were foreseen for the CTV. The implant resulted in

7 needles with 2 seeds, 1 needle with 1 seed, for a total of 15 seeds. This underlines the importance of having sparene edles before starting a procedure; C) Saggital view of the treatment planning; D) The fusion between preplanning PET and after treatment CT. An evident lesion growth between PET scan and intervention day

4.3 Interventional treatment description

Initially, we planned to treat lesions A and B, which were the most pertinent, in the same session. On the day of implantation, however, lesion A looked noticeably larger (about 2 × 3 cm), therefore we chose to treat just lesion A to guarantee there would be enough seeds to completely cover the target. We experienced a discrepancy between the actual lesion dimension and our treatment plan because of lesion expansion. As required by the protocol, we therefore intended to treat lesion B and monitor it closely during regular follow-up visits. We contoured the CTV directly on the skin after administering 20 ml of mepivacain + 1: 100,000 adrenalin along the lesion's perimeter.

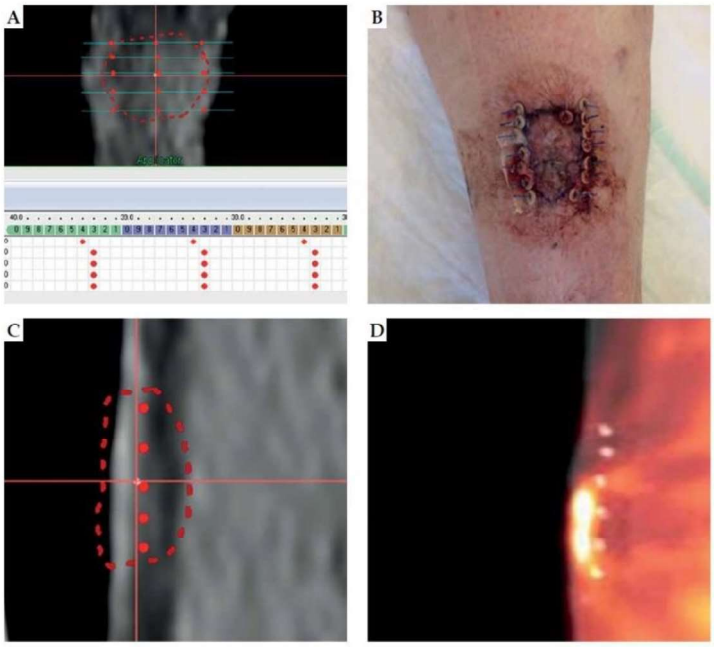

Figure 13 The treated lesion B that has grown from treatment planning session; B) The pretreatment planning session, 5 needles of 2 seeds spaced between each other of about 3-4 mm to account for lesion swelling were foreseen for the CTV. The implant resulted in 7 needles with 2 seeds, 1 needle with 1 seed, for a total of 15 seeds. This underlines the importance of having sparene edles before starting a procedure; C) Saggital view of the treatment planning; D) The fusion between preplanning PET and after treatment CT. An evident lesion growth between PET scan and intervention day

We then implanted the seeds using the Paris system, using a total of 8 applicators—7 loaded with 2 seeds and 1 with 1 seed—with an intra-seed wire distance of approximately 5 mm on a single plane, 7 parallels, and 1 perpendicular to sufficiently cover the CTV's

peripheral margin, as illustrated in Figure 14. Five seeds were produced as a result of the treatment's mismatch with the strategy. Following the implant, we ran a CT scan to confirm that the seeds were positioned inside the tumor in the proper geometrical orientation as intended. The differences between treating a lesion after it has grown and planning PET/CT are shown in Figures 13C and 13D. We want to stress the significance of this early CT scan verification because, in the event of unsatisfactory results, it is possible to correct treatment by moving any seed that is not where it should be or by inserting another seed or seeds for better coverage of the entire CTV. High frequency US imaging, however, is the most effective method of evaluating tumor extension throughout the implant operation. The seeds were removed after 15 days, after 95% of the radiation had been administered. Usually, the removal is done on day 15, and to administer 100% of the dose, another 15 days would be needed. Figure 15 shows an evident lesion shrinkage with a persistent minimal area of hyperkeratosis and in Figure 16 we show as a comparison the shrinkage of the untreated lesion B.

Following the treatment of lesion A for fifteen days, lesion B exhibited a discernible decrease in its nodular component, characterized by a persistent mild hyperkeratosis with perilesional erythema. According to the suspected minimal region of disease persistence, a dermatologist re-biopsied untreated lesion B and the remaining lesion A on the 28th day, as depicted in Figure 17.

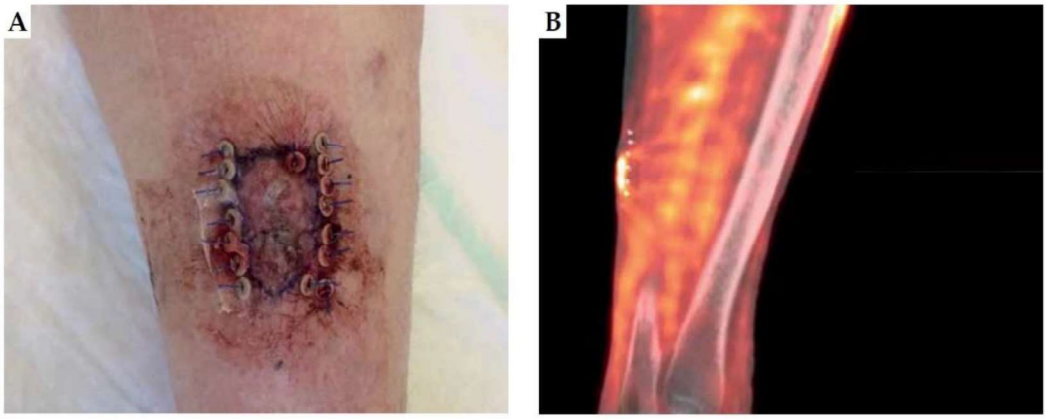

Figure 14 A) Final appearance of lesion A one day after treatment; B) Fusion between the pretreatment PET/CT and the CT performed after the implant

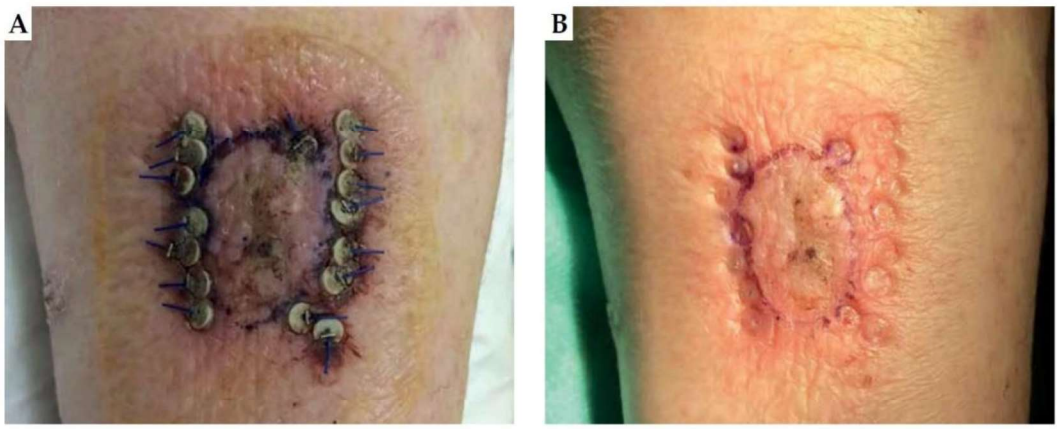

Figure 15 Appearance of lesion A at day 15 before (A) and immediately after (B) implant removal

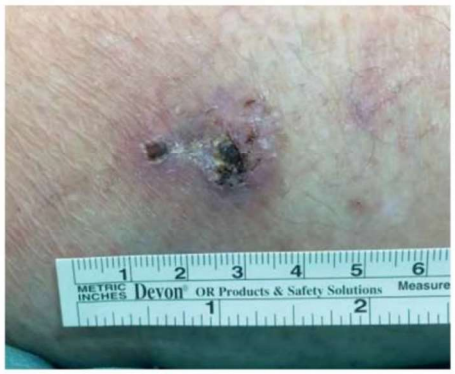

Figure 16 Modification of lesion B at 15th day after implant:marked reduction of its nodular component, with persisting mild hyperkeratosis with perilesional erythema

In the context of a potential new DaRT treatment, a biopsy of a third lesion (C) on the contralateral thigh seen in Figure 16 was carried out on the same day. Only lesion C showed a positive cSCC outcome. Both the treated lesion A and the untreated lesion B's histological examinations revealed no remaining cancerous cells. After the treatment of lesion A showed complete tumor remission and lesion B showed spontaneous regression, we made the decision to treat lesion C. However, in a combined evaluation with a dermatologist around 10 days prior to the scheduled DaRT treatment and 2.5 months after the implant, we discovered that lesion C was also in remission (as illustrated in Figure 18C). As a result, the planned treatment was canceled. 76 days following treatment, lesion A is seen on the left, B is in the middle, and lesion C is on the right in Figure 18.

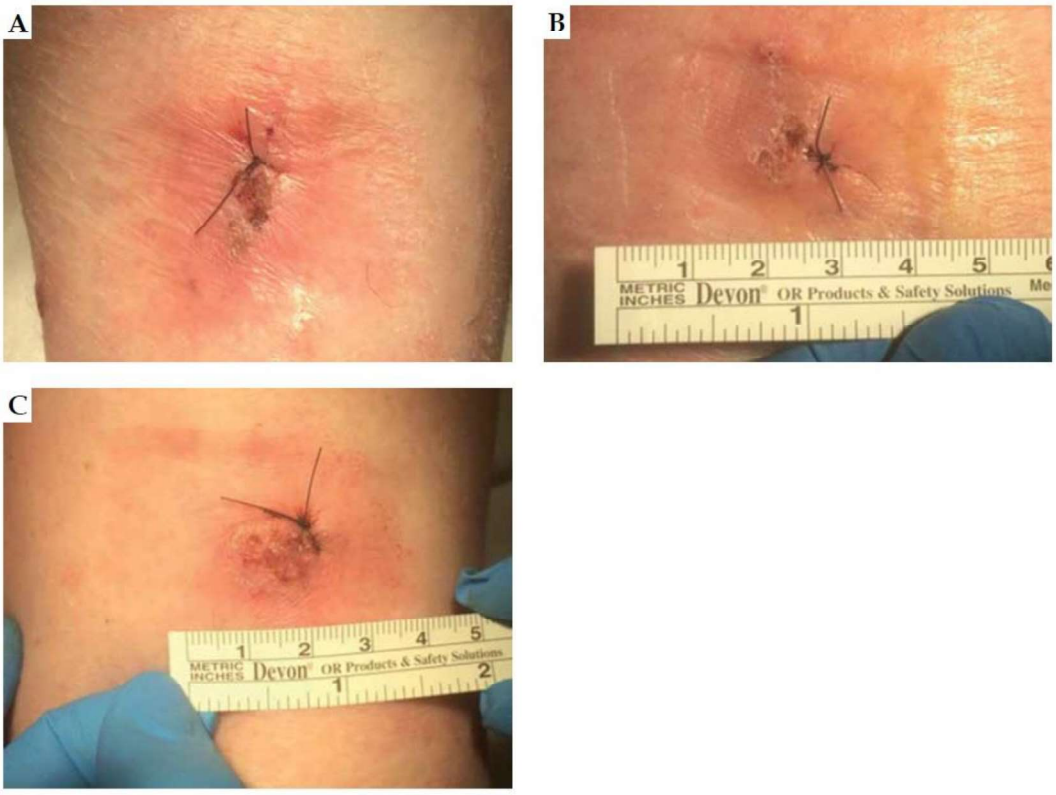

Figure 17 A) Re-biopsy on residual lesion A, in correspondence of suspected minimal area of persistence of disease; B) Re-biopsy of untreated lesion B; C) Biopsy of a third lesion, on the contra-lateral thigh, for a possible new DaRT treatment

At least two distant sites (B and C) showed evidence of an out-of-target tumor response, despite the patient achieving a complete response in the intended irradiation lesion (A left). Lesion C was on the opposite leg from lesion A, and lesion B was roughly 15 cm apart from lesion A. One year following therapy, untreated distant lesions spontaneously recede and the treated lesion remains completely in remission.

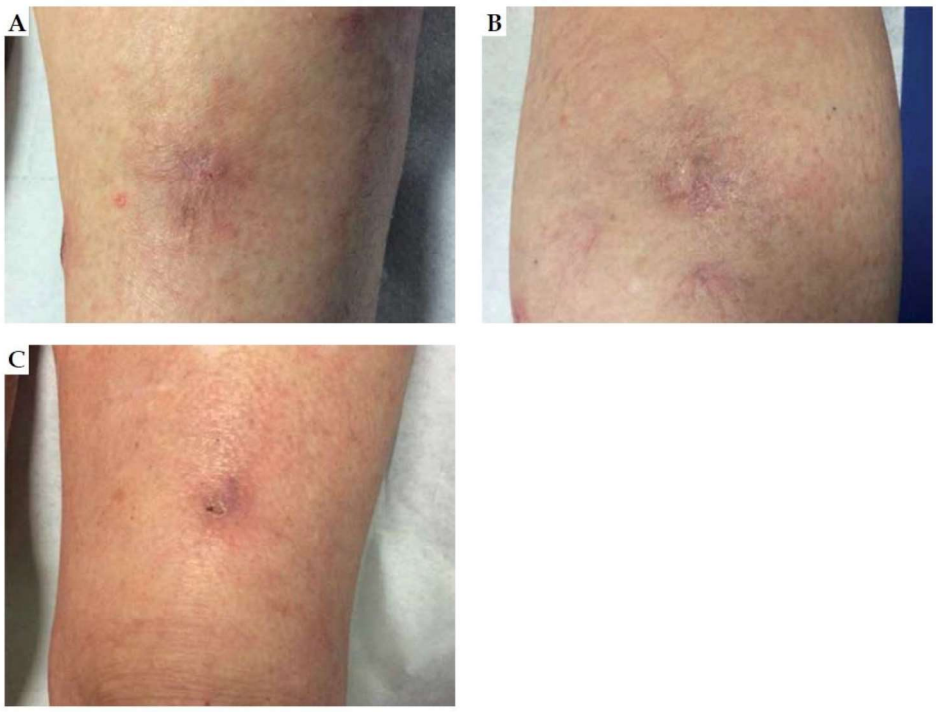

Figure 18 Appearance of lesion A, B, and C at day 76 after implant

In the 15 days following the implant, the patient's clinical reports indicated just a grade 1 erythema and minor, transient pain in the implant region. After the implant was removed, no further negative events happened.

4.4 Discussion

The mechanism underlying adverse events (AEs), which may be linked to an increased immune response triggered by high-dose radiation, remains poorly defined and unclear.

The abscopal effect is the subject of numerous theories. The first idea relates to leukemias and lymphomas; it is postulated that radiation therapy may cause the release of compounds harmful to lymphomas and prevent the synthesis and secretion of substances necessary for the growth of tumors to continue [48–50]. According to the second idea, local irradiation of solid tumors causes the release of cytokines (mitotic inhibitors) into the bloodstream, which in turn mediates a systemic anticancer impact. One example of such an inhibitor is tumor necrosis factor (TNF). The third theory proposes that the abscopal effect is immune-mediated: local radiotherapy would increase the activity of natural killer cells, and irradiation of a tumor at one site would cause the local release of circulating tumor antigens (CTA) and/or inflammatory factors that may mediate an increased immune response against unirradiated lesion that express similar tumor antigens [51]. Last but not least, the most intriguing theory—also known as "in vivo

vaccination"—postulates that local tumor destruction reveals tumoral antigens that are hidden yet capable of triggering systemic antitumor response[52, 53]. A growing body of research indicates that low immunogenic features in the tumor or a malfunction in the host systemic immunity may promote the development of cancer. The development of tumors is accompanied by anti-tumor immune-mediated mechanisms, and immunological monitoring is crucial for the management of cancer. The anti-tumor immune response is continuously reduced by tumor-derived immunosuppression.

As a result, an effective antitumor therapy may include a medication that boosts or restores immune system activity. According to recent research, radiation therapy can function as an immunostimulant, releasing danger signals like HMGB1 and producing immunogenic cell death, among other effects [54, 55]. Due to the inherent properties of high-LET alpha particles, which can cause a powerful in situ tumor ablation, DaRT treatment may be highly significant because it can more easily trigger an anti-tumor immune response than low-LET radiation, which is used in conjunction with traditional external beam radiation therapy (EBRT). Moreover, DaRT's removal of the tumor leaves the surrounding vasculature intact, allowing an inflow of immune cells to identify and eliminate the tumor cells. If validated, this capability may provide new opportunities for DaRT, including in a clinical setting where radiation therapy is typically thought to be extremely ineffective. For example, partial radioablation (debulking) with DaRT could activate the immune system in situations where standard irradiation techniques cannot deliver tumoricidal doses on the entire tumoral mass (prior irradiation, target difficulty, close proximity of organs at risk, multi-lesion diffused diseases, patient not able to sustain conventional fractionation). After that, the immune system would target the main mass as well as any other lesions farther away. By inhibiting immunosuppressive cells and utilizing immunoadjuvants, systemic anti-tumor immunity can be further enhanced [27].

One possible interpretation of our findings is that KA could be mistakenly diagnosed as cSCC.First reported in 1888, the KA is a mysterious tumor also known by the names "pseudotumor," "regressing tumor," and "self-healing SCC." Other names for this unique nosological phenomenon show that whereas KA seldom develops into an invasive form of SCC, it can in a significant proportion of instances spontaneously regress.[56, 57] It therefore occupies a gray area between benignity and malignancy, and numerous publications characterize it as a low-grade malignant SCC subtype. On the other hand, some medical professionals think that KA is essentially a benign lesion that has the potential to turn malignant and become typical SCC [58–60]. It is thought to have sprung from a hair follicle because of its triphasic nature (proliferative, stability, and regression), which closely resembles the stages of a hair follicle's cycle. SCC and KA are comparable in some aspects, including their cellular makeup. Numerous investigations show no discernible distinctions between them in terms of both histology and clinical presentation. Because of their regression time mismatch with the one reported for KA, which is between three and six months following the lesion's entire growth, the regression of untreated lesions B and C in our study can also be linked to an abscopal effect (AE) [61]. This is the

first instance of an adverse event (AE) in a patient with multiple synchronous cSCC and the first instance of an AE in a patient undergoing DaRT treatment, as far as we are aware. It was also because of this uncommon presentation of many synchronous lesions that we were able to witness this uncommon behavior in our patient. If we had been treating a patient with a single lesion, by definition, we would not have had any opportunity to observe an adverse event. characteristics with SCC, sharing comparable cellular traits. Numerous investigations show that there are no notable distinctions between them in terms of histology or clinical presentation. The regression of untreated lesions B and C in our study may also be linked to an abscopal effect (AE) due to a mismatch in their regression period with the one noted for KA, which is three to six months after the lesion has fully grown [61]. To the best of our knowledge, this is the first instance of an adverse event (AE) in a patient receiving DaRT therapy as well as the first instance of an AE in a patient with multiple synchronous cSCC. It was also because of this uncommon presentation of many synchronous lesions that we were able to witness this uncommon behavior in our patient. If we had been treating a patient with a single lesion, by definition, we would not have had any opportunity to observe an adverse event.

Based on our experience, we reported the first case of AE in cSCC in this study. When KA starts to show signs of SCC, it eventually loses its ability to regress spontaneously. Multiple synchronous forms of KA are extremely uncommon. Additionally, the time at which KA spontaneous regression occurs differs from the one we saw in our case, which was too short—about one month as opposed to three to six months. All of these data point to the possibility that radiation stimulates an abscopal effect, which is most likely mediated by the immune system. Our goal with the next DaRT treatments is to keep an eye on immune cells like T-lymphocytes as well as circulating soluble indicators. Even in individuals with solitary lesions, where an abscopal effect is by definition impossible to witness, the immune system's activation driven by radiation can be indirectly demonstrated by the largest increases from baseline in peripheral blood at different time periods or by induced denovo subpopulations. These data will reinforce recent discoveries about the use of radiation as an immune adjuvant in a variety of therapeutic settings, including advanced stage illnesses [52, 62]. Last but not least, while the DaRT approach is not particularly complex, it is still relatively new and, like other brachytherapy techniques, requires standardization and specialized training [63–66].

Chapter 5 Application of DaRT on prostate cancer

In the world, males are diagnosed with prostate cancer second most often after other types of cancer. In more affluent nations, where just 17% of men worldwide have prostate

cancer, it is the most common cancer among males, accounting for nearly two-thirds of all cases. Globally, incidence rates differ by almost 25 times, with the highest rates found in Australia/New Zealand, Northern America, Northern and Western Europe, and certain Caribbean countries, and the lowest rates found in Asia. The Caribbean and Southern and Middle Africa have the greatest mortality rates from prostate cancer, which is the fifth most common cause of cancer-related deaths globally [67].

Radiation therapy is an effective and well tolerated approach for appropriately selected patients with localized prostate cancer. Incremental advances in the delivery of radiotherapy over the last several decades have improved the ability to accurately target the prostate as well as escalate radiation dose, an essential component of optimal local control. Multiple prospective and retrospective studies demonstrate improved biochemical control by increasing conventionally fractionated radiation dose from 64Gy to 81Gy [68–71].

Despite the advances in radiotherapeutic techniques, biochemical failure remains troublesome with rates of varying between 10-50% depending on risk grouping [72]. While some failures occur due to presence of distant metastatic or regional disease, a component of these failures, particularly if identified early may be local and potentially amenable to salvage therapy. Salvage therapies are varied and include SRP, brachytherapy, cryotherapy and more recently HIFU. Toxicities vary depending on the modality and are a limitation to current salvage approaches.

SRP is challenging given the extent of post-radiation peri-prostatic fibrosis that can develop making dissection difficult. As such, complication rates following SRP are higher than in the primary treatment setting. The most frequent complications reported include incontinence, impotence, bladder neck contractures and rectourethral fistulae. Published series report post-SRP incontinence rates as high as 25-80% [73–75]. Erectile dysfunction rates are also high with published post-SRP impotence rates of 80-100%.

Less radical urologic ablation procedures such as cryotherapy and HIFU are somewhat better tolerated than SRP, however also have limiting toxicities. Cryotherapy uses argon and helium in freeze-thaw cycles down to -40º Celsius to destroy tissue typically in conjunction with a warming device in the urethra. HIFU destroys tissue using low frequency, high energy ultrasound to heat tissue to 65-85º Celsius inducing coagulative necrosis Reported series of salvage cryotherapy have reported urinary incontinence and impotence rates of 10-15% [76, 77]. Also noted in these series are rectourethral fistulae rates of 1-3%. Salvage HIFU reported rates of incontinence are 20-50% in reported series and in one series 5% rectourethral fistula rate [78, 79].

Salvage brachytherapy using either LDR or HDR have been reported since the 1990s. Grado et al and Beyer et al initially reported 5-year bRFS rates of 30 and 50% [80, 81].

Since that time, improvements have been made in both technique and patient selection which have improved efficacy with 3-5y bRFS rates of 60-75% in more recent series [82, 83]. In addition, toxicity rates with brachytherapy appear favorable with reported incontinence rates of 10-15%. Urethral strictures and radiation proctitis occur as well in rates ranging for 5-10%. The selection of brachytherapy approach has not been found to influence outcome or toxicity in a recent analysis.

Alpha particles are created during the process of alpha decay and are made up of two protons and two neutrons bonded together. With energy ranges between 3 and 7 MeV, which are far higher than those of any other typical radiation, they are a highly ionizing form of particle radiation. However, their poor depth of penetration and relatively high bulk have limited their usage in radiation therapy.

The first chance to treat solid tumors with an alpha particle-based interstitial radiation device is provided by DaRT seeds. The instrument is composed of a wire that has been infused with a predetermined amount of a main radioisotope (Ra-^{224}). The optimal method for inserting this wire is image-guidance directly into the tumor tissue. Inside the tumor, a decay chain of short-lived alpha emitters is created when the parent isotope decays. The increased vascularity in the tumor facilitates the diffusion of these alpha emitters. Based on pre-clinical investigations that are discussed below and the irregular and tumor-confined structural features of tumor vascularity, it is thought that tumor tissue benefits more from alpha particle diffusion than normal tissue does.

5.1 Technical Aspect of DaRT insertion in prostate

One major technical issue when considering DaRT insertion in focal prostate cancer is precision and accuracy of seeds insertion due to the small range of alpha particles in tissue. The killing dose of 10 Gy is reached within 2.5 mm apart from seed location so it becomes crucial to have control over the seed insertion site. In order to cover a focal tumor with dimensions ranging from 0.5 to 2.5 cm in diameter about 20-200 ^{224}Ra seeds are required. Due to this high variability and numerosity of seeds a safe, precise and accurate insertion and verification procedure must be enstabilished. In this thesis we outline some preliminary projects, experiments and safety evaluation for this technique development and to ensure an accuracy of seeds positioning.

5.2 Prostate biopsy and seeds positioning parallelism

In order to solve the issue of safety and accuracy for DaRT positioning we take inspiration and start from our experience in prostate biopsy. Most recent advancements in prostate biopsy employ mp-MRI fusion with transperineal ultrasound to guide precise biopsy when

focal lesion that requires higher attention are found in the prostate. The transperineal procedure for biopsy is essentially the same procedure that we are going to use for DaRT seeds insertion, but requiring higher precision as described above.

The diagnostic accuracy of biopsy techniques among which the most important are in-bore MRI biopsy, Ultrasound-guided biopsies Cognitive and fusion-targeted biopsy is still under debate. A meta- analysis comparing the main techniques, which included 43 studies with a total of 2497 patients found no significant advantage of any particular technique for csPCa detection. Another meta-analysis, comparing only fusion- and cognitive-TBx using 1714 men from nine studies, concluded there was a trend toward improved csPCa detection rates for fusion-TBx; however, this was not statistically significant. Because the studies included in both meta-analyses had small sample sizes and were subject to significant heterogeneity, the results need to be interpreted with caution.

However among the biopsy-naïve men enrolled in the multicenter PRECISION trial [84], csPCa was detected in 12%, 60%, and 83% of the men with PIRADS 3, 4, and 5 lesions, in comparison with 13%, 46%, and 82% in the fusion cohort of Costa et al, respectively. These results suggest that in-bore biopsies may be a superior targeting approach, potentially reducing the numbers of false-negative biopsies and indolent cancers detected.

In a more recent study, Costa et al [85] evaluated biopsy results from a mixed (prior negative and biopsy naïve) cohort, with MRGB (n = 103) performing significantly better than TBx combined with SBx (N = 300), reporting csPCa detection rates of 61 and 47%, respectively. The same group, using a partly overlapping cohort, found significantly more Grade Group upgrading when matching radical prostatectomy histopathology to biopsy results in the TBx/SBx group (27.7%) compared to MRBG (13%). The results of these studies show a clear advantage in diagnostic accuracy for MRGB. However, it is difficult to say if these results can be extrapolated to general practice, considering both trials originated from a single centre and have a non-randomised and retrospective design.

Considering the research data described above the objective of our future work is to improve the csPCa detection rate of Fusion Biopsy by using electromagnetic needle guidance and improved patient positioning (stirrup device in figure 19 and phantom US probe during exam). The outcome would be to minimize upgrading when matching radical prostatectomy histopatology to biopsy results aiming to obtain MRBG results of 13%.

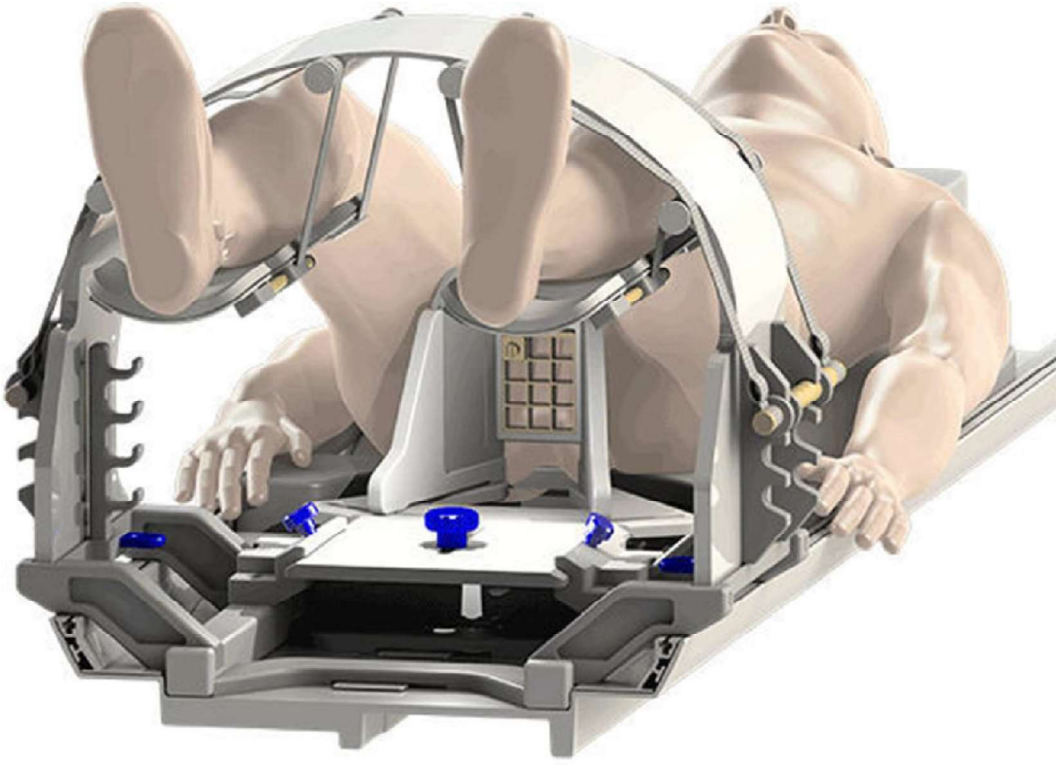

Figure 19 MRI safe stirrup device for transperineal biopsy or DaRT procedure interventions

The same procedure hypothesized for biopsy can be applied to DaRT seeds insertion that follow the same transperineal access and that we describe below.

5.2.1 DaRT seeds insertion procedure for Prostate Cancer

We briefly describe here the procedure for ^{224}-Ra seeds insertion in prostate which is equal to the procedure for the already common 125 – I insertion.

Patients enrolled in the experimental protocol CTP-PRST-00 receive focal transrectal interstitial prostate salvage therapy guided by ultrasound using the DaRT technique. The procedure is performed according to the latest standards provided by the international guidelines GEC-ESTRO ACROP[41] .

The outpatient procedure is performed under anesthesia in the dorsal lithotomy position with a Foley catheter for urethral visualization. The transrectal ultrasound probe is positioned after rectal irrigation and is secured to the operating table through the stirrup device shown in figure 19. A template is used to position the needles containing Alpha DaRT seeds according to the treatment plan that is shown in detail in figure 20.

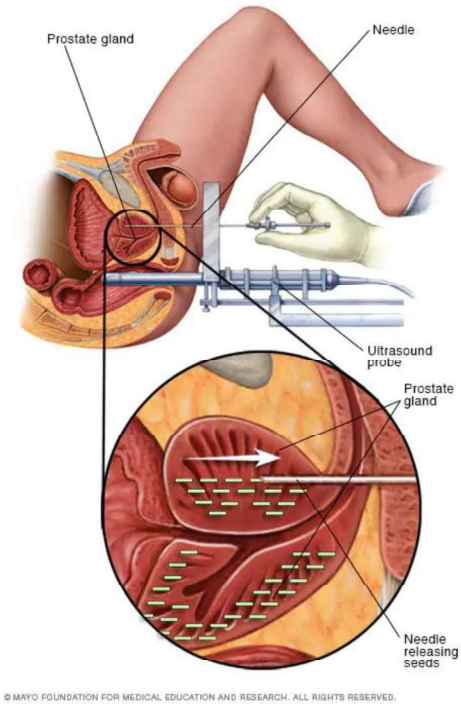

Figure 20 Transrectal US guide for transperineal needle access in prostate DaRT procedure

The needles used are similar to those used for I-125 therapies and are shown in Figure 21. The needle size is 18 cm, and the Ra-^{224} seeds are positioned at the tip. The needle can accommodate a single seed or multiple seeds arranged in a row and contiguous.

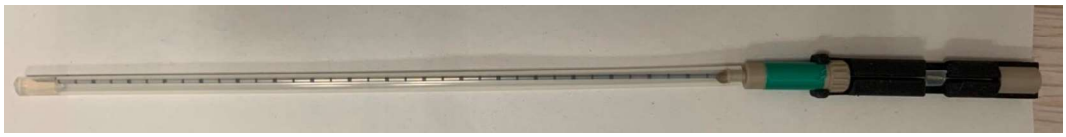

Figure 21 DaRT 18 cm prostate needle applicator

The Alpha DaRT seeds for prostate treatment have higher activity compared to those used for skin and oral cavity lesion treatment. Each seed has an Ra-^{224} activity of 0.185 MBq (5 µCi). The seeds are positioned using a dedicated template with holes spaced 4 mm apart in a hexagonal approach. The positioning is based on a pre-implant treatment plan executed on dedicated Treatment Planning (TPS) software. The seeds are implanted with a minimum safety distance of 5 mm from the urethra and rectum to reduce the likelihood of migration. After seed implantation, a CT scan is performed to verify seed positioning and dosimetric calculations as depicted in figure 22 in a typical 125-I treatment. We will detail simulations with possible issues performed on phantom for DaRT seeds positioning and verification.

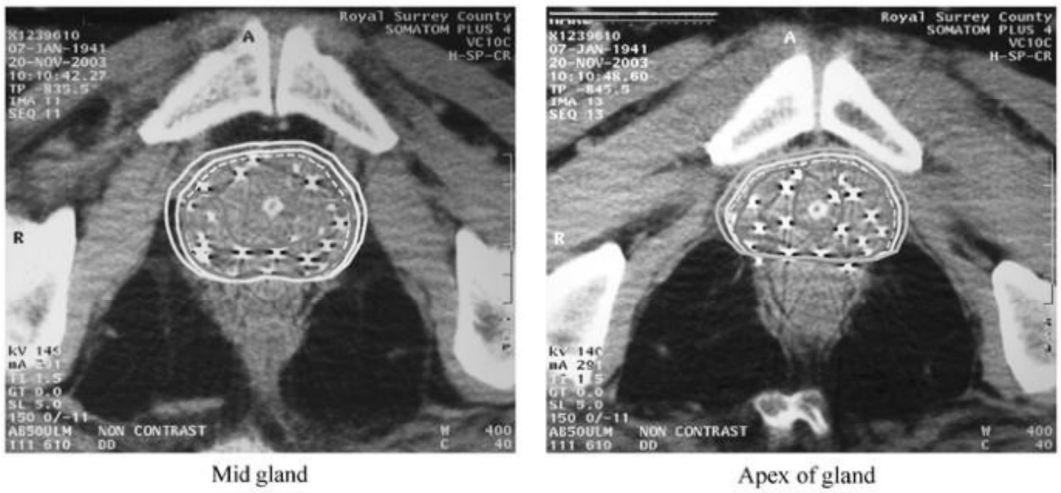

Figure 22 Example of a 125-I brachytherapy treatment for whole gland treatment of prostate cancer

As described earlier, Ra-^{224} seeds (half-life 3.7 days) release Rd-^{220} (half-life ~1 min), which in turn leads to a cascade of decay events resulting in the production of alpha particles that damage the DNA of tumor cells.

The maximum allowable size for focal prostate treatment according to the research protocol CTP-PRST-00 is 3 cm. Following treatment simulation using TPS to achieve 10 Gy coverage of the CTV with a 4 mm spacing between seed filaments in a hexagonal array, a maximum of 173 seeds is obtained. Adding an additional 15% reserve seeds as recommended by AlphaTau, a final maximum number of 199 seeds is obtained. Considering an activity of 0.185 MBq per seed (5 μCi/seed), an instant activity for prostate treatment of 37 MBq/patient (1000 μCi/patient) is achieved.

For accurate accounting of the sources actually used, the medical physics specialist records the applicators used during the procedure (applicator code and number of seeds/applicator) on a dedicated electronic form, the total number of seeds inserted into the tumor, and their overall activity. As an additional check, the medical physics specialist inspects the surrounding area with a Geiger counter to rule out the presence of any dispersed seeds.

Since the patient must undergo anesthesia according to the clinical protocol, depending on the type of anesthesia and clinical conditions, the patient may be discharged after a minimum of 6 hours from the procedure or be admitted for overnight clinical observation and managed according to international guidelines.

All patients receive a document containing behavioral guidelines upon discharge.

5.2.2 Displacement issue for focal treatment

In this section, we present the outcomes of our experimental investigations pertaining to the potential challenges encountered when addressing specific lesions as opposed to employing the comprehensive treatment approach previously elucidated. Focal lesions are exclusively detectable with magnetic resonance imaging (MRI), while they remain imperceptible in computed tomography (CT) scans. The DaRT process involves the fusion of MRI and ultrasound images acquired using a transrectal probe. However, it is possible for displacements to occur throughout the procedure as a result of the transrectal probe that provides imaging guidance throughout the treatment.

In order to address this matter, we conducted an assessment using a Multi-Modality Male Pelvic Phantom (Mod. 048A - CIRS, Norfolk, VA, USA). This anthropomorphic phantom is specifically designed for simulating the anatomical region in question, as depicted in Figure 23. Our evaluation focused on the procedure of inserting seeds and the subsequent displacement resulting from the transrectal insertion of ultrasounds.

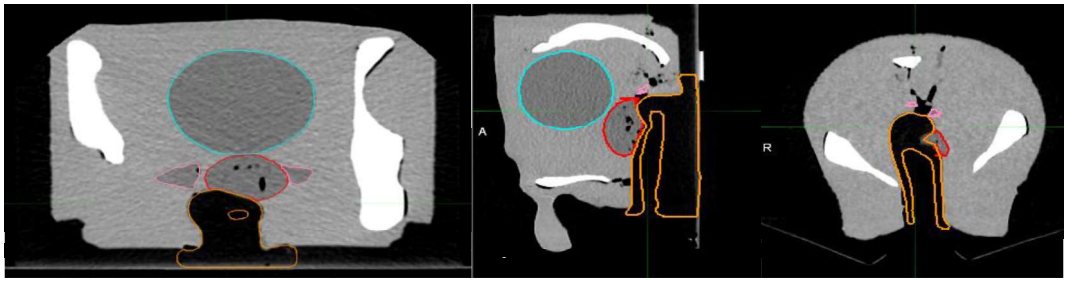

Figure 23 CT scan of the CIRS phantom simulating the pelvis region with the contouring of the prostate (red), seminal vescicles (pink), bladder (light blue) and rectum (orange): transverse plan (a), sagittal plan (b) and coronal plan (c).

The insertion of a single DaRT seed was conducted in accordance with the protocol outlined in section 5.2.1. Subsequently, a verification CT scan was performed immediately after the treatment, utilizing a probe put into the phantom. Subsequently, the ultrasonic probe is detached in order to ascertain the extent of displacement induced by the probe on the prostate gland at the site of seed implantation.

Figure 24 depicts the fusion of a computed tomography (CT) scan conducted on a phantom immediately following the placement of an inert DaRT seed within the core region of a simulated prostate gland. The evaluation of the displacement of the DaRT seed site yields a measurement of 0.8 cm.

Nevertheless, a potential theoretical resolution to the current problem involves modifying the methodology of treatment planning by utilizing the stirrup device depicted in figure 19 during the MRI employed to visualize the focal lesion using a 3D printed mold resembling an ultrasound probe that would be inserted into the patient's rectum to mimic the treatment position.

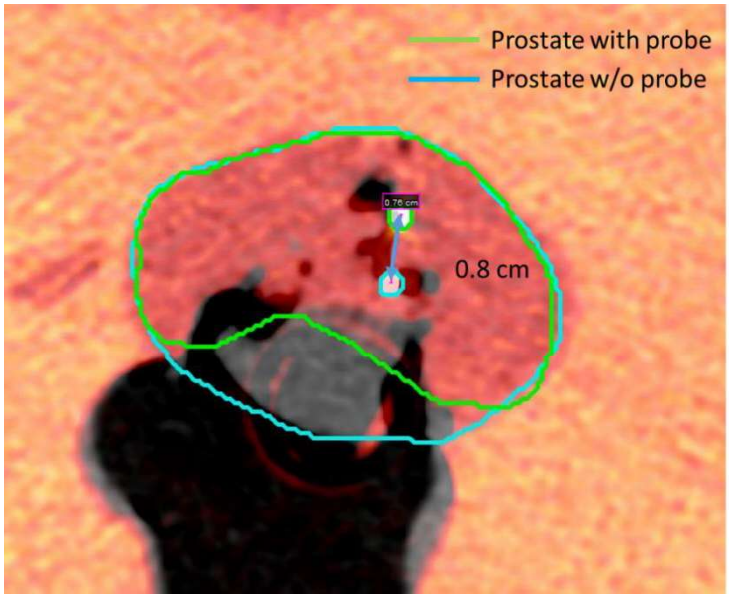

Figure 24 Prostate gland phantom with DaRT implant with and without transrectal ultrasound probe. Seeds displacement is quantified in 0.8 cm

Chapter 6 Improvements of DaRT technique in SCC treatments

Published in: Cancers

Giacomo Feliciani, Salvatore Roberto Bellia, Massimo Del Duca, Giorgio Mazzotti, Manuela Monti, Ignazio Stanganelli, Yona Keisari, Itzhak Kelson, Aaron Popovtzer, Antonino Romeo and Anna Sarnelli,

A new approach for a safe and reproducible seeds positioning for Diffusing Alpha-emitters Radiation Therapy of squamous cell skin cancer: a feasibility study.

doi: 10.3390/cancers14010240

The purpose of this chapter is to discuss how to use an external radio-opaque template in the Diffusing Alpha-emitters Radiation Therapy (DaRT) technique's pre-planning and treatment stages[86]. This device would help to determine the proper number of sources for tumour coverage ac-counting for subcutaneous invasion and augmenting DaRT safety. The procedure will be carried out in a first phase on phantom and then applied to a clinical case. A typical DaRT procedure workflow comprises steps like tumor measurements and delineation, source number assessment, and therapy administration. As first step an adhesive fiberglass mesh (spaced by 2 mm) tape was applied on the skin of the patient and employed as frame of reference. A Physician contoured the lesion and marked the entrance points for the needles with a radio opaque ink marker. According to the radio opaque marks and metabolic uptake the clinical target volume was defined and with a commercial brachytherapy TPS it was possible to simulate and adjust the spatial seeds distribution. After the implant procedure a CT is performed again to check the agreement between simulations and seeds positions. With the procedure described above it was possible to simulate a DaRT procedure on phantom in order to train physicians and subsequently apply the novel approach on patient outlining the major issues involved in the technique. The present work innovates and supports DaRT technique for the treatment of cutaneous cancers improving its efficacy and safety.

6.1 Introduction

The current standard of care for cutaneous squamous cell skin carcinoma (cSCC) is surgical excision, which involves removing the tumour while leaving a margin of healthy skin. If surgery is not an option or is not viable, gamma or beta-based external beam radia-tion

and brachytherapy can be used as alternatives. However, these techniques may be ineffective due to hidden tumour invasion or radio resistance [87].

The Diffusing Alpha-emitters Radiation Therapy (DaRT) is a novel brachytherapy technique employing ^{224}Radium (Ra-^{224}) enriched seeds releasing short-lived al-pha-emitting atoms into the tumour [8, 18]. The efficacy of DaRT was proven in a series of preclinical studies on tumours with different histology such as squamous cell, colon, breast, pancreas, lung and prostate carcinoma [22, 27, 88]. Furthermore, Tumor abolition by alpha DaRT resulted in activation of specific anti tumor immunity [27, 89] and an abscopal effect in one patient [90].

This technique improves standard gamma-based brachytherapy treatments with the high Relative Biological Effectiveness of alpha particles and higher control of dose to or-gans at risk in the surroundings of the implant area [91]. In fact, alpha radiation is gener-ally more effective against tumors achieving a higher degree of cell killing probability for a given absorbed dose and being insensitive to poor oxygenation of tissues [92]. The main obstacle in employing alpha radiation for cancer treatments relies in the short range of alpha particles in liquid and solid medium (i.e. water and tissue). DaRT overcomes this limitation because Ra-^{224} incorporated on the surface of implantable seeds decays directly into the tumor in ^{220}Radon and its progeny which migrate away from the implant site, in virtue of recoil energy and its gaseous nature, for an average distance of 2.5 mm [93].

DaRT is to all intent an interstitial brachytherapy technique, notoriously an effective and short procedure, and it is clinically employed for the treatment of cutaneous squa-mous cell carcinoma (cSCC) at our center Istituto Romagnolo per lo Studio dei Tumori "Dino Amadori" - IRST IRCCS (Meldola, FC, Italy). The technique has recently concluded the “first in man” clinical trial N. CTP-SCC-00 (NCT03015883) with promising results showing a complete response tumor rate 78.6% and a partial response rate of 21.4% of the lesions [94]. The pre-treatment step, which includes the need to predict the correct number of Ra-^{224} seeds to implant based on tumor dimension and shape days in advance, is a major issue in completing this operation. To date no commercial treatment planning sys-tem exist to calculate alpha particle dose and the source estimation is generally performed geometrically on the patient's skin and/or on a preplanning CT or PET/CT, with the sources spaced about 4-5 mm apart to reach the killing dose in the entire Clinical Target Volume (CTV). We propose and describe how to use an external radio-opaque template in the pre-planning and treatment phases of the DaRT technique to help evaluate the correct number of sources for cSCC. The template is used to aid clinicians in visualizing lesions and their eventual subcutaneous expansion during the pre-planning procedure. It is also utilized on treatment day to ensure that the sources are properly inserted into the tumor and to monitor for tumor progression.To begin, the treatment will be carried out on a phantom to demonstrate the efficacy of the entire approach as well as the physician training required to safely implanting the seeds without the involvement of the patient.

Second, the procedure will be demonstrated on a patient to demonstrate its utility in clinical settings.

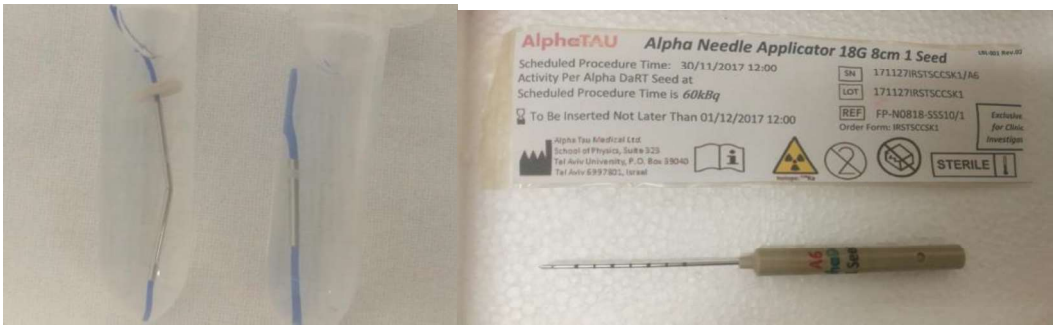

Figure 25 2-cm and 1-cm long DaRT ^{224}-Ra source seeds (left) and needle applicator for seeds insertion (right).

6.2 Materials and Methods

6.2.1 Overview

DaRT technique relies on the implantation of 1-cm long Ra-^{224} loaded seeds directly in the tumour site through needle applicators as shown in Figure 25. After a little training on the specific applicator, a physician should be able to perform the treatment with ease. Except for implantation near major blood vessels, where a safety margin of 1 cm should be used, the operation has no specific contraindications. Each seed is loaded with an average activity of 2 µCi and can be ordered in series up to a length of 6 cm. A standard DaRT technique workflow is presented in Figure 26, which includes phases such as tumour measurements and delineation, source number, evalua-tion, and treatment delivery. In the pre-treatment phase, the radiation oncologist draws the CTV directly on the patient's skin with a surgical pen and marks the needle insertion locations with a ruler, as shown in Figure 26A. Inter-distance among insertion point is about 4-5 mm to assure a tumour dose coverage of at least 10 Gy. The patients subse-quently undergo a CT or PET/CT scan to check lesion subcutaneous extension (Figure. 26B). Another seed number estimation is accomplished geometrically on a commercial TPS for traditional brachytherapy in collaboration with a medical physicist (Figure 26C). After sources arrival seeds implantation is performed manually by radiation oncologist (Figure 26D). Finally a CT scan after implant is performed to check for correct displacement of the sources.

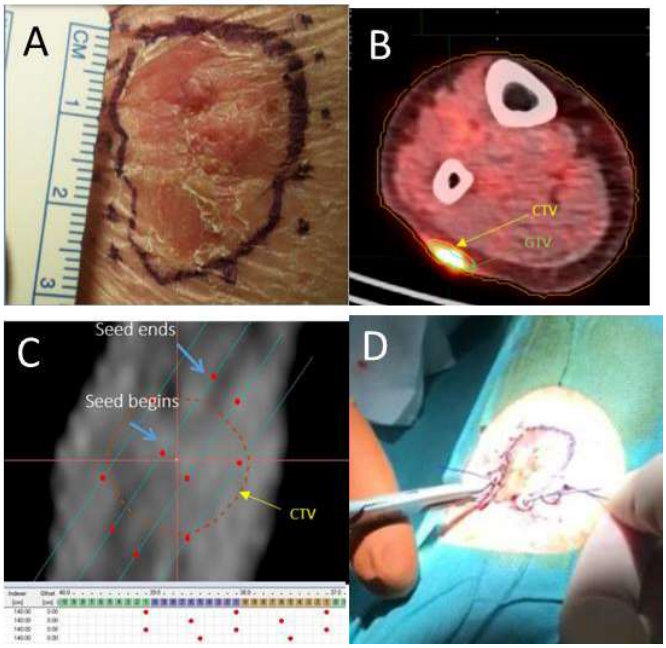

Figure 26 (upper-left) Lesion is contoured by the physician directly on the skin of the patient and insertion points are theoretically marked with surgical blue ink. (upper-right) Gross Tumor Volume (GTV) of the lesion is contoured on a PET/CT scan and Clinical Tumor Volume is obtained as expansion of 3 mm of the GTV in order to consider for microscopic tumor invasion and eventual patient swell during intervention. (bottom-left) Commercial TPS is employed to geometrically evaluate the number of seeds needed for full tumour coverage. (bottom-right) Seeds implantation is performed by the radiotherapist.

6.2.2 Template based planning phase 1: phantom training

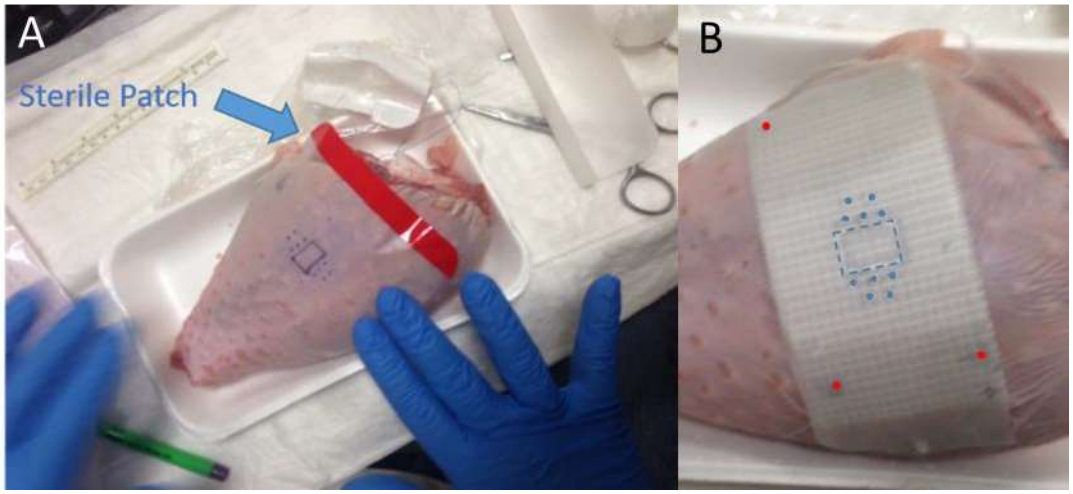

Figure 27 Phantom lesion is contoured by the physician with surgical blue ink and a transparent sterile patch is su-perimposed (indicated in figure by the blue arrowl). (b) adhesive fiberglass mesh is applied over the

patch in order to re-draw the lesion with radio-opaque ink (marked in blue) and the localization points used as reference points (marked with red dots)

Figure 27 shows a phantom (turkey leg) that replicates a human skin surface. In Figure 27A a Brachytherapist draws a superficial rectangular lesion with a surgical marker that simulates a squamous skin cancer visible on the phantom's surface, as well as 5 nee-dle insertion and exit points spaced about 4-5 mm and displaced on two planes to simu-late a subcutaneous lesion invasion of about 6 mm (two ^{224}-Ra loaded seeds disposed on planes one over the other can safely cover a maximum of 8 mm depth with tumor killing dose of 10 Gy in case of subcutaneous tumor invasion). The lesion and its environs are covered with a sterile transparent patch, which is then covered with an adhesive fiber-glass mesh tape (Figure 27B). To achieve a smooth surface, a layer of silk sticky tape was ap-plied to the mesh. The physician uses a silver-based non-toxic radio-opaque ink to copy the contouring done on the skin on this surface. Finally, three radio-opaque spots are drawn on the fiberglass mesh and then tattooed onto the skin with black ink in order to reapply the tape on implant day, as indicated in Figure 27B by the red points.

A pre implant CT is then performed where the radio opaque trace will be clearly visi-ble together with the insertion points. Using the commercial Treatment Planning System (TPS) Oncentra Brachy, Elekta, Stockholm, Sweden, contouring of the hypothetical lesion CTV is performed on CT by following the radio-opaque trace and extending it to a depth of 6 mm to simulate a deep lesion. Geometrical planning is finally performed using the TPS software following the radio opaque insertion points. Planned seeds are implanted and phantom is scanned again on CT. Pre and post implant CT are then fused for coverage verification through MIMmaestro imaging suite (MIM Software Inc., Beachwood, Ohio, US). The Fusion process is performed employing a bounding box around the lesion and its radio-opaque trace.

6.2.3. Template based planning phase 2: patient application

The technique outlined in the previous paragraph and represented in Figure 27 is now executed on the patient. The patient is first visited by a brachytherapist, who draws the le-sion with a surgical marker. After that, a sterile patch was put, followed by fiberglass mesh. On the day of the intervention, the lesion drawing is duplicated on the fiberglass mesh with radio-opaque ink, and tattoos are applied to the skin as a frame of reference to reposition the mesh tape. At this time, a PET/CT scan is performed to determine the extent of the tumor's subcutaneous extension, which is done by contouring the gross tumor volume (GTV) on the TPS and expanding it by 3 mm to define the CTV. The template is adjusted if there is a mismatch with the original drawing. The new template is reapplied to the lesion on the day of the intervention, aligning the radiopaque sites with the tattoos. This allows the physician to mark the correct extension of the CTV on the skin and ade-quately cover it with planned sources.

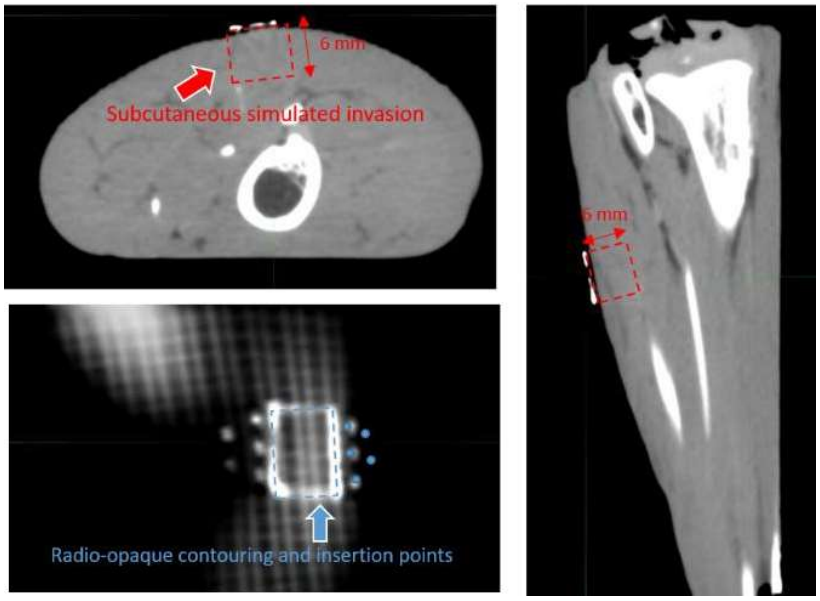

Figure 28 Details of the visibility of the radio-opaque ink in axial coronal and sagittal plane

6.3 Results

6.3.1. Template based planning phase 1: phantom training

Following the phantom preparation described in the template-based planning: phantom training section and displayed in Figure 27, the CT image of the phantom is pre-sented in Figure 28, highlighting the visibility of the fiberglass mesh and the lesion drawn with silver-based ink. The needle applicator's entrance and exit locations are visible near to the lesion. On the TPS needle applicators are represented as catheters for the conven-tional brachytherapy planning whereas ^{224}-Ra seeds extremities are simulated by active source points spaced of 1 cm as depicted in Figure 29A. Geometrical arrangement of the seeds is done keeping 2 mm from the surface of the skin and a distance between seeds of a maximum of 5 mm as shown in Figure 29A and 29B. The distribution of needles and seeds required to properly cover the target from a superficial point of view (coronal view) is shown in Figure 29A, whereas the axial view of the phantom and the need for a second plane below the first to completely cover the red contoured target area is shown in Figure 29B. In Figure 29C needles are inserted according to the drawing and the phantom is scanned again and fused with the planning CT. In Figure 30 a detail of the first and second seed layer is shown. The first seed layer is measured to be at 0.26 cm from the surface whereas the second layer is at 0.6 cm from the surface and 0.34 cm from the first layer.

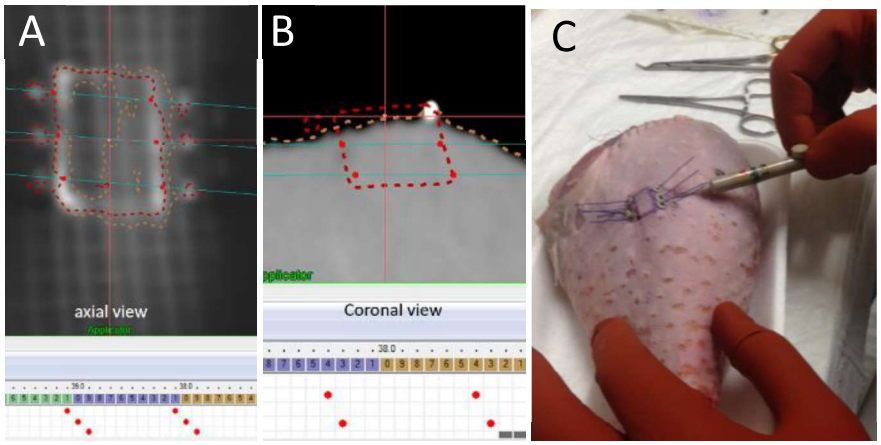

Figure 29 (**A**) CT coronal view of the radio-opaque contouring of the lesion with needles' insertion and exit points. (**B**) Axial view of the lesion contoured with dotted red line and brachytherapy catheters reconstruction simulating needles displacement. (C) Detail of the needle insertion procedure.

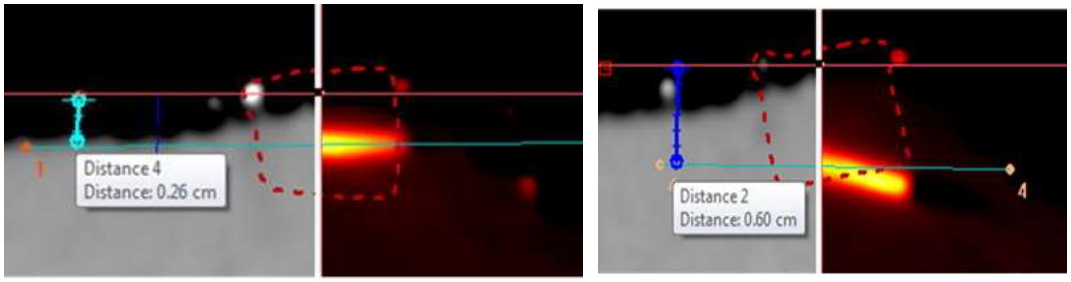

Figure 30 Pre- and post-implant phantom CT fusion, showing the first (**A**) seed insertion plane at 0.26 cm from the surface and the second (**B**) insertion plane at 0.6 cm from the surface.

6.3.2. Template based planning phase 2: patient application

As shown in Figure 31, the previously mentioned technique was performed on the patient. The contouring of the patient lesion GTV in Figure 31A is depicted in green, with its 3 mm isotropic expansion to account for tumor margins shown in blue denoting the CTV. The mesh tape was placed upon the patch and the skin-drawn lesion reported with the radiopaque ink on the mesh as shown in Figure 31B. Localization point marks were placed at the corner of the tape and CT scan was performed. In Figure 32A the CTV drawn directly on the skin by the physician is shown in blue and subsequently, in Figure 32B three seeds are planned in order to cover the blue target. The physician now outlines a second CTV in red based on the information from the PET/CT scan about the tumor's subcutaneous expansion. The discrepancy between the visible CTV and the PET/CT based CTV is greater than 6 mm as shown Figure 32C, result-ing in a shift in the number of seeds required to completely cover the target from 3 to 4. The CTV drawn on the skin even accounting for

large margins (3 mm) doesn't consider sub-cutaneous invasion nor possible tumour growth that may led to dangerous target miss and possible recurrence.

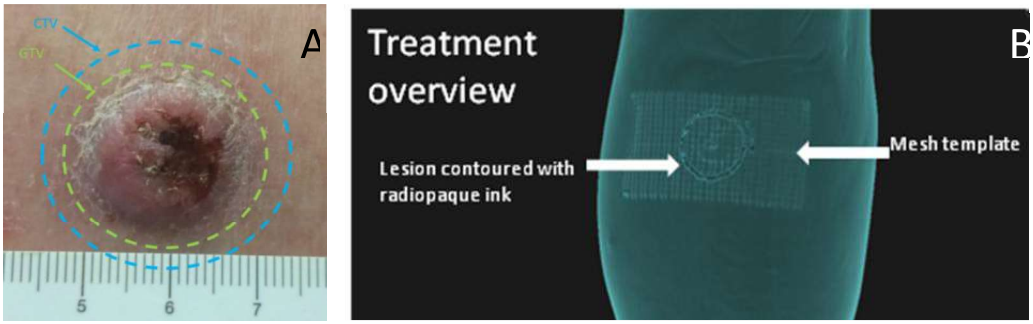

*Figure 31 (**A**) GTV contouring is shown in green, with its enlargement to a 3mm CTV shown in blue. (**B**) 3D rendering of the radio-opaque template with details of lesion CTV and mesh template.*

As a result of these considerations, the required number of sources and seed displacement were updated evaluating the amount of space to fully cover the PET/CT based CTV directly on the radio-opaque mesh as shown in Figure 32D. In this case an expansion of the CTV of 6 mm is required (correspondent to 3 steps on the radio-opaque mesh). The physical template is then updated according to the previous considerations and displayed in Figure 33.

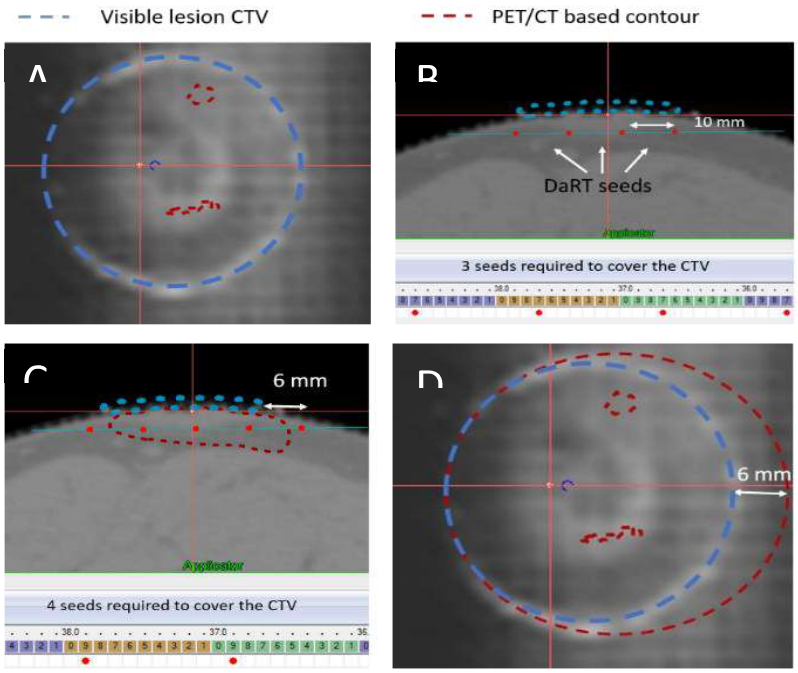

Figure 32 (A) Visible CTV drawn with the radio-opaque marker by the physician highlighted in blue over the radio-opaque trace. (B) Geometrical planning on CT with the TPS with the 1cm long DaRT seeds represented by red dots. The cover-age of blue CTV is achieved with 3 seeds (C) The PET/CT-based CTV is depicted in red alongside the blue CTV, indi-cating subcutaneous tumor invasion and the necessity for four DaRT seeds for

proper lesion coverage. (D) Final esti-mation of the CTV is drawn on the template mesh in order to update the physical template.

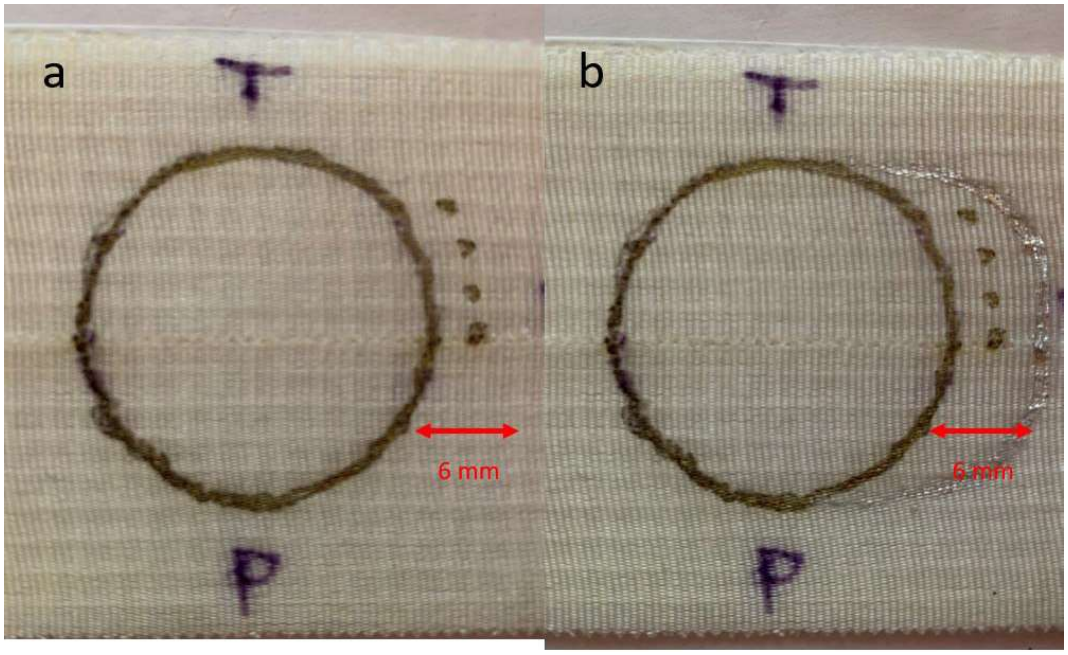

Figure 33 Template update after subcutaneous invasion considerations.

6.4 Discussion & Conclusions

The DaRT technology recently completed the "first in man" clinical study N. CTP-SCC-00 (NCT03015883), and the Food and Drug Administration of the United States awarded it the "Breakthrough Device Designation." As previously stated by Arazi et al., this technique is based on the direct insertion of ^{224}-Ra loaded sources into the tumor.

Alpha particles are extremely effective in destroying cancer cells in comparison to standard photon-based techniques, however their limited range in tissue represent a strong limitation for their application in clinical setting. Consequence and requirement to employ particle based radiotherapy is a great precision in target localization and dose delivery. An advantage of this technique relies in the fact that alpha particles are deposited directly into the tumor without the need of large and very expensive technological facilities to accelerate hadrons such for particle external beam radiotherapy. However, precision in target coverage is still a central issue for DaRT technique. We demonstrated step by step the feasibility of a template based procedure in phantom and subsequently applied it on patient leading to several major benefits in treatment precision and safety.

The direct visualization of the lesion on CT via the radio-opaque template will assist physicians and medical physicists in better evaluating real lesion borders and, as a result,

a better estimation of the number of sources required to achieve full tumor coverage while minimizing needle insertions, as shown in Figures 29A and 32B and C.

Furthermore, by comparing the naked eye and PET/CT based lesion CTV, millimetric sized subcutaneous lesion expansions that are very difficult to see can be analyzed. Even increasing the naked eye-based GTV by 3 mm to account for tumour subcutaneous extension, the lesion is not totally encompassed by the CTV for other 5 mm, as shown in Figure 32. This difference may appear irrelevant for photon based techniques but it becomes crucial when dealing with alpha particles where a maximum distance of 2.5 mm is tolerated to assure 10 Gy tumour killing dose coverage. Without template guidance in this case, it's very likely that a target miss will occur during the implant, with probable tumor relapse as a result.

In Figure 31 we can observe image fusion between pre and post implant CT on phantom where we tried to force radio-opaque ink marks superimposition. Although we were able to evaluate the intervention results with sub millimetric precision using this comparison, we were only able to achieve fair results using standard fusion approaches due to lesion swell generated by the insertion of the sources. This is the study's primary limitation, as the swell will be significantly more prominent in patients. Advanced fusion approaches, such as elastic registrations, can be used to alleviate this problem, but it is outside the scope of this work. Regardless of this difficulty, it is still pos-sible to determine that seeds were planted and spaced at a maximum of 4 mm apart.

The procedure's flexibility in considering tumour subcutaneous extension and poten-tial growth is the procedure's last benefit. It is possible to extrapolate quantitatively the modifications required for tumor coverage using the TPS and, as a result, update the template. New tumor borders and needle insertion locations coordinates are derived from the radio-opaque mesh and used to update the physical template, eliminating target misses and optimizing seeds positioning, as shown in Figure 32D and 33.

The DaRT's safety and precision were improved in this study, which included a de-tailed description of physician training on phantom and clinical applications. In particu-lar dealing with subcutaneous extension of the tumour the use of a template may avoid dangerous target miss and ensure complete dose coverage.

Chapter 7 Future directions & Conclusions

7.1 Long Term Follow up of cSCC Patients Treated with DaRT

28 lesions in 23 patients were eligible and treated per protocol. Treatment was delivered via a percutaneous interstitial technique with placement of the radioactive DaRT to encompass the tumor volume with margin. Tumor control was assessed using serial radiographic imaging or clinical assessments. The median follow-up time was 28 months following treatment. Complete response to the Ra-^{224} DaRT treatment was observed in 22 lesions (22/28; 79%); 6 lesions (6/28, 21%) manifested a partial response. Among the 22 lesions with a CR, 9 (41%) developed a subsequent local relapse at the site of DaRT implantation at a median time of 6.2 months (range: 2.8-35.4 months). The 2-year local progression-free survival (PFS) probability at the implanted site was 50% (95% Confidence Interval, CI: 28-68%) for complete responders. The 2-year overall survival rates post-DaRT implantation was 65% (95% CI: 42%-81%) among all patients and was 77% (95% CI: 50%-91%) among complete responders. Despite prior therapy among these recurrent, locally advanced tumors, Ra-^{224} DaRT treatment was well tolerated and associated with excellent 2-year tumor control outcomes. A pivotal US trial for marketing approval is already underway.

7.2 Conclusions

For numerous years, brachytherapy has heavily depended on the use of radioactive beta and gamma sources. However, the introduction of novel sources with enhanced radio-biological potency holds significant potential in offering substantial advantages to patients afflicted with solid tumors that have a bleak prognosis. Additional studies are currently being conducted to assess the feasibility and safety of DaRT therapy in the treatment of various solid tumors, including pancreatic tumors, as well as recurring breast, prostate, and vulvar malignancies.

Previous preclinical investigations have indicated that the utilization of DaRT therapy in combination with immunotherapy has the potential to exploit the immune response. In this thesis, it was seen that a single patient had an immunological response characterized by a decrease in disease severity at other tumor sites while undergoing DaRT therapy for one of the symptomatic lesions. Notably, this response occurred in the absence of any concurrent therapies. Trials are currently being developed to examine the concept that the combination of DaRT, tailored to a specific lesion, with immunotherapy could enhance

the immune response in cancers with oligometastases, as compared to immunotherapy alone.

The utilization of radium-223 in systemic alpha radiotherapy has demonstrated a notable increase in survival rates among individuals with castrate-resistant prostate cancer. This observed benefit may be attributed, at least in part, to an immunological mechanism that has the potential to impede the advancement of metastatic disease. Based on the findings of the present pilot investigation, it is important to note that final conclusions regarding response rates cannot be drawn. However, it is worth mentioning that these data have been included as part of our initial observations for this limited-scale pilot project. The preliminary findings indicate that alpha particle brachytherapy has the potential to open up new ways for further research in the treatment of malignancies that were previously believed to be resistant to radiotherapy and unresponsive to treatment. The aforementioned results also suggest that DaRT therapy is a viable method that should be classified as a form of reirradiation. This strategy shows potential for reducing patient morbidity in comparison to stereotactic body radiation therapy and other external beam approaches.

Currently, there is an initiation of Phase I/II prospective studies in patient groups that are more homogeneous. These studies focus on individuals who have recurrent and persistent local disease, and have already undergone surgery and external beam radiation therapy. The forthcoming investigations will incorporate enhanced evaluation of delayed adverse effects, with further focus on secondary objectives encompassing tumor control outcomes.

The potential benefits of utilizing tailored DaRT therapy to exploit the immune system's capabilities in treating a specific lesion are noteworthy and warrant investigation through future prospective trials. While conventional treatment planning approaches were employed for these patients, it is evident that incorporating radio-biologic-based treatment planning and novel techniques will be advantageous and essential in the integration of alpha source brachytherapy with known therapies. The implementation of these emerging treatment paradigms, together with the integration of this therapy with current therapeutic techniques, necessitates the execution of comprehensive prospective trials on a wider scale.

In this thesis we outlined our experience in treating the first patients with this brand new technique. The theoretical biokinetic model developed for patient safety was successfully tested for 3 patients. In the end we developed a new technique for increasing the accuracy of DaRT treatment on superficial cutaneous squamous cell carcinomas.

Bibliography

1. Lassmann M, Eberlein U (2018) Targeted alpha-particle therapy: imaging, dosimetry, and radiation protection. Ann ICRP 47:187–195. https://doi.org/10.1177/0146645318756253

2. Eberlein U, Scherthan H, Bluemel C, et al (2016) DNA Damage in Peripheral Blood Lymphocytes of Thyroid Cancer Patients After Radioiodine Therapy. J Nucl Med 57:173–179. https://doi.org/10.2967/jnumed.115.164814

3. Eberlein U, Nowak C, Bluemel C, et al (2015) DNA damage in blood lymphocytes in patients after (177)Lu peptide receptor radionuclide therapy. Eur J Nucl Med Mol Imaging 42:1739–1749. https://doi.org/10.1007/s00259-015-3083-9

4. Eberlein U, Peper M, Fernández M, et al (2015) Calibration of the γ-H2AX DNA double strand break focus assay for internal radiation exposure of blood lymphocytes. PLoS One 10:e0123174. https://doi.org/10.1371/journal.pone.0123174

5. Sgouros G, Roeske JC, McDevitt MR, et al (2010) MIRD Pamphlet No. 22 (abridged): radiobiology and dosimetry of alpha-particle emitters for targeted radionuclide therapy. J Nucl Med 51:311–328. https://doi.org/10.2967/jnumed.108.058651

6. Kratochwil C, Bruchertseifer F, Rathke H, et al (2018) Targeted Alpha Therapy of mCRPC with 225Actinium-PSMA-617: Swimmer-Plot analysis suggests efficacy regarding duration of tumor-control. J Nucl Med. https://doi.org/10.2967/jnumed.117.203539

7. Parker C, Nilsson S, Heinrich D, et al (2013) Alpha emitter radium-223 and survival in metastatic prostate cancer. N Engl J Med 369:213–223. https://doi.org/10.1056/NEJMoa1213755

8. Arazi L, Cooks T, Schmidt M, et al (2007) Treatment of solid tumors by interstitial release of recoiling short-lived alpha emitters. Phys Med Biol 52:5025–5042. https://doi.org/10.1088/0031-9155/52/16/021

9. Garrett JD (1980) Table of isotopes (seventh edition): C. M. LEDERER and V. S. SHIRLEY, ed., (Wiley-Interscience, New York, 1978; xx-1523-A64 pp). Nucl Phys A 342:528–529. https://doi.org/https://doi.org/10.1016/0375-9474(80)90559-X

10. Godwin HA (2001) The biological chemistry of lead. Curr Opin Chem Biol 5:223–227. https://doi.org/https://doi.org/10.1016/S1367-5931(00)00194-0

11. Leggett RW (1993) An age-specific kinetic model of lead metabolism in humans. Environ Health Perspect 101:598–616. https://doi.org/10.1289/ehp.93101598

12. Blank M, Lavie G, Mandel M, et al (2004) Antimetastatic activity of the photodynamic agent hypericin in the dark. Int J cancer 111:596–603. https://doi.org/10.1002/ijc.20285

13. Amemiya Y, Miyahara J (1988) Imaging plate illuminates many fields. Nature 336:89–90. https://doi.org/10.1038/336089a0

14. Kiss MZ, Sayers DE, Zhong Z (2002) Comparison of X-ray detectors for a diffraction enhanced imaging system. Nucl Instruments Methods Phys Res Sect A Accel Spectrometers, Detect Assoc Equip 491:280–290. https://doi.org/https://doi.org/10.1016/S0168-9002(02)01125-7

15. Bourgeois D, Moy JP, Svensson SO, Kvick Å (1994) The point-spread function of X-ray image-intensifiers/CCD-camera and imaging-plate systems in crystallography: assessment and consequences for the dynamic range. J Appl Crystallogr 27:868–877. https://doi.org/10.1107/S0021889894004048

16. Lucy L ~B. (1974) An iterative technique for the rectification of observed distributions. \aj 79:745. https://doi.org/10.1086/111605

17. Richardson WH (1972) Bayesian-Based Iterative Method of Image Restoration$\ast$. J Opt Soc Am 62:55–59. https://doi.org/10.1364/JOSA.62.000055

18. Cooks T, Arazi L, Schmidt M, et al (2008) Growth retardation and destruction of experimental squamous cell carcinoma by interstitial radioactive wires releasing diffusing alpha-emitting atoms. Int J Cancer 122:1657–1664. https://doi.org/10.1002/ijc.23268

19. Cooks T, Al E (2009) BIOLOGY CONTRIBUTION LOCAL CONTROL OF LUNG DERIVED TUMORS BY DIFFUSING ALPHA-EMITTING ATOMS RELEASED FROM INTRATUMORAL WIRES LOADED WITH RADIUM-224. Biol Contrib 74:966–973. https://doi.org/10.1016/j.ijrobp.2009.02.063

20. Stabin M (2006) Nuclear medicine dosimetry. Phys Med Biol 51:R187. https://doi.org/10.1088/0031-9155/51/13/R12

21. (1993) Age-dependent doses to members of the public from intake of radionuclides: Part 2. Ingestion dose coefficients. A report of a Task Group of Committee 2 of the International Commission on Radiological Protection. Ann ICRP 23:1–167

22. Lazarov E, Arazi L, Efrati M, et al (2012) Comparative In Vitro Microdosimetric Study of Murine- and Human-Derived Cancer Cells Exposed to Alpha Particles. Radiat Res 177:280–287. https://doi.org/10.1667/RR2664.1

23. Grimard L, Esche B, Lamothe A, Spaans JN (2009) Interstitial brachytherapy in the management of persistent head and neck disease after definitive external beam radiation therapy. Brachytherapy 8:284–289. https://doi.org/10.1016/j.brachy.2008.12.007

24. Bartochowska A, Wierzbicka M, Skowronek J, et al (2012) High-dose-rate and pulsed-dose-rate brachytherapy in palliative treatment of head and neck cancers. Brachytherapy 11:137–143. https://doi.org/10.1016/j.brachy.2011.09.006

25. Reitkopf-Brodutch S, Confino H, Schmidt M, et al (2015) Ablation of experimental colon cancer by intratumoral 224Radium-loaded wires is mediated by alpha particles released from atoms which spread in the tumor and can be augmented by chemotherapy. Int J Radiat Biol 91:179–186. https://doi.org/10.3109/09553002.2015.959666

26. Confino H, Hochman I, Schmidt M, et al (2015) Tumor ablation by intratumoral Ra-224- loaded wires induces anti-tumor immunity against experimental metastatic tumors. Cancer Immunol Immunother 64:191–199. https://doi.org/10.1007/s00262-014-1626-8

27. Confino H, Schmidt M, Efrati M, et al (2016) Inhibition of mouse breast adenocarcinoma growth by ablation with intratumoral alpha-irradiation combined with inhibitors of immunosuppression and CpG. Cancer Immunol Immunother 65:1149. https://doi.org/10.1007/s00262-016-1878-6

28. Milrot E, Jackman A, Flescher E, Sherman L (2012) Enhanced killing of cervical cancer cells by combinations of methyl jasmonate with cisplatin , X or alpha radiation. Invest new Drug DOI 10.100: https://doi.org/10.1007/s10637-012-9870-2

29. Mole RH (1953) Whole Body Irradiation—Radiobiology or Medicine? Br J Radiol 26:234–241. https://doi.org/10.1259/0007-1285-26-305-234

30. Abuodeh Y, Venkat P, Kim S (2016) Systematic review of case reports on the abscopal effect. Curr Probl Cancer 40:25–37. https://doi.org/10.1016/j.currproblcancer.2015.10.001

31. Rees GJG, Ross CMD (1983) Abscopal regression following radiotherapy for adenocarcinoma. Br J Radiol 56:63–66. https://doi.org/10.1259/0007-1285-56-661-63

32. Siva S, Macmanus MP, Martin RF, Martin OA (2015) Abscopal effects of radiation therapy : A clinical review for the radiobiologist. Cancer Lett 356:82–90. https://doi.org/10.1016/j.canlet.2013.09.018

33. Cotter S, Dunn GP, Collins KM, Et A (2011) Abscopal effect in a patient with metastatic merkel cell carcinoma following radiation therapy: Potential role of induced antitumor immunity. Arch Dermatol 147:870–872

34. Maverakis E, Cornelius LA, Bowen GM, et al (2015) Metastatic Melanoma – A Review of Current and Future Treatment Options. 516–524. https://doi.org/10.2340/00015555-2035

35. Stamell EF, Wolchok JD, Gnjatic S, et al (2013) The Abscopal Effect Associated With a Systemic Anti-melanoma Immune Response. Radiat Oncol Biol 85:293–295. https://doi.org/10.1016/j.ijrobp.2012.03.017

36. Bramhall RJ, Mahady K, Peach AHS (2014) Spontaneous regression of metastatic melanoma e Clinical evidence of the abscopal effect. Eur J Surg Oncol 40:34–41.

https://doi.org/10.1016/j.ejso.2013.09.026

37. Barker CA, Postow MA (2014) Combinations of Radiation Therapy and Immunotherapy for Melanoma : A Review of Clinical Outcomes. Radiat Oncol Biol 88:986–997. https://doi.org/10.1016/j.ijrobp.2013.08.035

38. Espenel S, Vallard A, Rancoule C, et al (2017) Critical Reviews in Oncology / Hematology Melanoma : Last call for radiotherapy. Crit Rev Oncol / Hematol 110:13–19. https://doi.org/10.1016/j.critrevonc.2016.12.003

39. Ebner DK, Tinganelli W, Helm A, et al (2017) The immunoregulatory potential of particle radiation in cancer therapy. Front Immunol 8:1–8. https://doi.org/10.3389/fimmu.2017.00099

40. Fernandez-Gonzalo R, Baatout S, Moreels M (2017) Impact of particle irradiation on the immune system: From the clinic to mars. Front Immunol 8:1–7. https://doi.org/10.3389/fimmu.2017.00177

41. Guinot JL, Rembielak A, Perez-Calatayud J, et al (2018) GEC-ESTRO ACROP recommendations in skin brachytherapy. Radiother Oncol 126:377–385. https://doi.org/10.1016/j.radonc.2018.01.013

42. Tagliaferri L, Kovács G, Aristei C, et al (2019) Current state of interventional radiotherapy (brachytherapy) education in Italy: results of the INTERACTS survey. J Contemp Brachytherapy 11:48–53. https://doi.org/10.5114/jcb.2019.83137

43. Kovács G, Tagliaferri L, Valentini V (2017) Is an Interventional Oncology Center an advantage in the service of cancer patients or in the education? The Gemelli Hospital and INTERACTS experience. J Contemp Brachytherapy 9:497–498. https://doi.org/10.5114/jcb.2017.72603

44. Lancellotta V, Kovács G, Tagliaferri L, et al (2019) The role of personalized Interventional Radiotherapy (brachytherapy)in the management of older patients with non-melanoma skin cancer. J Geriatr Oncol 10:514–517. https://doi.org/10.1016/j.jgo.2018.09.009

45. Lancellotta V, Kovács G, Tagliaferri L, et al (2018) Age Is Not a Limiting Factor in Interventional Radiotherapy (Brachytherapy) for Patients with Localized Cancer. Biomed Res Int 2018:1–10. https://doi.org/10.1155/2018/2178469

46. Popovtzer A (2017) Alpha Radiation Emitters Device for the Treatment of Squamous Cell Carcinoma. https://clinicaltrials.gov/ct2/show/NCT03015883 1–5

47. Khan L, Choo R, Breen D, et al (2012) Recommendations for CTV margins in radiotherapy planning for non melanoma skin cancer. Radiother Oncol 104:263–266. https://doi.org/10.1016/j.radonc.2012.06.013

48. Hendry JH, Moore J V (1979) The Radiobiology of Human Cancer Radiotherapy. Br J Cancer 40:175

49. Antoniades J, Brady LW, Lightfoot DA (1977) Lymphangiographic demonstration of

the abscopal effect in patients with malignant lymphomas. Int J Radiat Oncol Biol Phys 2:141–147

50. Rees GJ (1981) Abscopal regression in lymphoma: a mechanism in common with total body irradiation? Clin Radiol 32:475–480

51. Uchida A, Mizutani Y, Nagamuta M, Ikenaga M (1989) Effects of X-ray irradiation on natural killer (NK) cell system. I. Elevation of sensitivity of tumor cells and lytic function of NK cells. Immunopharmacol Immunotoxicol 11:507–519. https://doi.org/10.3109/08923978909005381

52. Demaria S, Formenti SC (2012) Radiation as an immunological adjuvant: current evidence on dose and fractionation. Front Oncol 2:1–7. https://doi.org/10.3389/fonc.2012.00153

53. Keisari Y (2017) Tumor abolition and antitumor immunostimulation by physico-chemical tumor ablation. Front Biosci 310–347

54. Perez CA, Fu A, Onishko H, et al (2009) Radiation induces an antitumour immune response to mouse melanoma. Int J Radiat Biol 85:1126–1136. https://doi.org/10.3109/09553000903242099

55. Gameiro SR, Jammeh ML, Wattenberg MM, et al (2014) Radiation-induced immunogenic modulation of tumor enhances antigen processing and calreticulin exposure, resulting in enhanced T-cell killing. Oncotarget 5:403–416. https://doi.org/10.18632/oncotarget.1719

56. Sanchez Yus E, Simon P, Requena L, et al (2000) Solitary keratoacanthoma: a self-healing proliferation that frequently becomes malignant. Am J Dermatopathol 22:305–310

57. Beham A, Regauer S, Soyer HP, Beham-Schmid C (1998) Keratoacanthoma: a clinically distinct variant of well differentiated squamous cell carcinoma. Adv Anat Pathol 5:269–280

58. Hodak E, Jones RE, Ackerman AB (1993) Solitary Keratoacanthoma Is a Squamous-Cell Carcinoma: Three Examples with Metastases. Am J Dermatopathol 15:

59. Mandrell JC, Santa Cruz D (2009) Keratoacanthoma: hyperplasia, benign neoplasm, or a type of squamous cell carcinoma? Semin Diagn Pathol 26:150–163

60. Weedon DD, Malo J, Brooks D, Williamson R (2010) Squamous cell carcinoma arising in keratoacanthoma: a neglected phenomenon in the elderly. Am J Dermatopathol 32:423–426. https://doi.org/10.1097/DAD.0b013e3181c4340a

61. Cassarino DS, De Rienzo DP, Barr RJ (2006) Cutaneous squamous cell carcinoma : a comprehensive clinicopathologic classification. J Cutan Pathol 33:261–279

62. Heguy A, Demaria S, Cooper B, et al (2018) Radiotherapy induces responses of lung cancer to CTLA-4 blockade. Nat Med 24:1845–1851. https://doi.org/10.1038/s41591-018-0232-2

63. Autorino R, Vicenzi L, Tagliaferri L, et al (2018) A national survey of AIRO (Italian Association of Radiation Oncology) brachytherapy (Interventional Radiotherapy) study group. J Contemp Brachytherapy 10:254–259. https://doi.org/10.5114/jcb.2018.76981

64. Tagliaferri L, Kovács G, Autorino R, et al (2016) ENT COBRA (Consortium for Brachytherapy Data Analysis): Interdisciplinary standardized data collection system for head and neck patients treated with interventional radiotherapy (brachytherapy). J Contemp Brachytherapy 8:336–343. https://doi.org/10.5114/jcb.2016.61958

65. Tagliaferri L, Budrukkar A, Lenkowicz J, et al (2018) Ent cobra ontology: the covariates classification system proposed by the Head & Neck and Skin GEC-ESTRO Working Group for interdisciplinary standardized data collection in head and neck patient cohorts treated with interventional radiotherapy (brachythera. J Contemp Brachytherapy 10:260–266. https://doi.org/10.5114/jcb.2018.76982

66. Tagliaferri L, Pagliara MM, Boldrini L, et al (2017) INTERACTS (INTErventional Radiotherapy ACtive Teaching School) guidelines for quality assurance in choroidal melanoma interventional radiotherapy (brachytherapy) procedures. J Contemp Brachytherapy 9:287–295. https://doi.org/10.5114/jcb.2017.68761

67. Sung H, Ferlay J, Siegel RL, et al (2021) Global Cancer Statistics 2020: GLOBOCAN Estimates of Incidence and Mortality Worldwide for 36 Cancers in 185 Countries. CA Cancer J Clin 71:209–249. https://doi.org/10.3322/caac.21660

68. Al-Mamgani A, van Putten WLJ, Heemsbergen WD, et al (2008) Update of Dutch multicenter dose-escalation trial of radiotherapy for localized prostate cancer. Int J Radiat Oncol Biol Phys 72:980–988. https://doi.org/10.1016/j.ijrobp.2008.02.073

69. Dearnaley DP, Jovic G, Syndikus I, et al (2014) Escalated-dose versus control-dose conformal radiotherapy for prostate cancer: long-term results from the MRC RT01 randomised controlled trial. Lancet Oncol 15:464–473. https://doi.org/10.1016/S1470-2045(14)70040-3

70. Kuban DA, Tucker SL, Dong L, et al (2008) Long-term results of the M. D. Anderson randomized dose-escalation trial for prostate cancer. Int J Radiat Oncol Biol Phys 70:67–74. https://doi.org/10.1016/j.ijrobp.2007.06.054

71. Zietman AL, Bae K, Slater JD, et al (2010) Randomized trial comparing conventional-dose with high-dose conformal radiation therapy in early-stage adenocarcinoma of the prostate: long-term results from proton radiation oncology group/american college of radiology 95-09. J Clin Oncol Off J Am Soc Clin Oncol 28:1106–1111. https://doi.org/10.1200/JCO.2009.25.8475

72. Roach M 3rd, Hanks G, Thames HJ, et al (2006) Defining biochemical failure following radiotherapy with or without hormonal therapy in men with clinically localized prostate cancer: recommendations of the RTOG-ASTRO Phoenix Consensus Conference. Int J Radiat Oncol Biol Phys 65:965–974.

https://doi.org/10.1016/j.ijrobp.2006.04.029

73. Gontero P, Marra G, Alessio P, et al (2019) Salvage Radical Prostatectomy for Recurrent Prostate Cancer: Morbidity and Functional Outcomes from a Large Multicenter Series of Open versus Robotic Approaches. J Urol 202:725–731. https://doi.org/10.1097/JU.0000000000000327

74. Mandel P, Steuber T, Ahyai S, et al (2016) Salvage radical prostatectomy for recurrent prostate cancer: verification of European Association of Urology guideline criteria. BJU Int 117:55–61. https://doi.org/10.1111/bju.13103

75. Yuh B, Ruel N, Muldrew S, et al (2014) Complications and outcomes of salvage robot-assisted radical prostatectomy: a single-institution experience. BJU Int 113:769–776. https://doi.org/10.1111/bju.12595

76. Ismail M, Ahmed S, Kastner C, Davies J (2007) Salvage cryotherapy for recurrent prostate cancer after radiation failure: a prospective case series of the first 100 patients. BJU Int 100:760–764. https://doi.org/10.1111/j.1464-410X.2007.07045.x

77. Li Y-H, Elshafei A, Agarwal G, et al (2015) Salvage focal prostate cryoablation for locally recurrent prostate cancer after radiotherapy: initial results from the cryo on-line data registry. Prostate 75:1–7. https://doi.org/10.1002/pros.22881

78. Crouzet S, Blana A, Murat FJ, et al (2017) Salvage high-intensity focused ultrasound (HIFU) for locally recurrent prostate cancer after failed radiation therapy: Multi-institutional analysis of 418 patients. BJU Int 119:896–904. https://doi.org/10.1111/bju.13766

79. Murat F-J, Poissonnier L, Rabilloud M, et al (2009) Mid-term results demonstrate salvage high-intensity focused ultrasound (HIFU) as an effective and acceptably morbid salvage treatment option for locally radiorecurrent prostate cancer. Eur Urol 55:640–647. https://doi.org/10.1016/j.eururo.2008.04.091

80. Grado GL, Collins JM, Kriegshauser JS, et al (1999) Salvage brachytherapy for localized prostate cancer after radiotherapy failure. Urology 53:2–10. https://doi.org/10.1016/s0090-4295(98)00492-0

81. Beyer DC (1999) Permanent brachytherapy as salvage treatment for recurrent prostate cancer. Urology 54:880–883. https://doi.org/10.1016/s0090-4295(99)00241-1

82. Burri RJ, Stone NN, Unger P, Stock RG (2010) Long-term outcome and toxicity of salvage brachytherapy for local failure after initial radiotherapy for prostate cancer. Int J Radiat Oncol Biol Phys 77:1338–1344. https://doi.org/10.1016/j.ijrobp.2009.06.061

83. Wong WW, Buskirk SJ, Schild SE, et al (2006) Combined prostate brachytherapy and short-term androgen deprivation therapy as salvage therapy for locally recurrent prostate cancer after external beam irradiation. J Urol 176:2020–2024. https://doi.org/10.1016/j.juro.2006.07.008

84. Kasivisvanathan V, Rannikko AS, Borghi M, et al (2018) MRI-Targeted or Standard Biopsy for Prostate-Cancer Diagnosis. N Engl J Med 1767–1777. https://doi.org/10.1056/nejmoa1801993

85. Jager A, van Riel LAMJG, Postema AW, et al (2022) An optimized prostate biopsy strategy in patients with a unilateral lesion on prostate magnetic resonance imaging avoids unnecessary biopsies. Ther Adv Urol 14:17562872221111410. https://doi.org/10.1177/17562872221111410

86. Feliciani G, Bellia SR, Del Duca M, et al (2022) A New Approach for a Safe and Reproducible Seeds Positioning for Diffusing Alpha-Emitters Radiation Therapy of Squamous Cell Skin Cancer: A Feasibility Study. Cancers (Basel) 14:. https://doi.org/10.3390/cancers14010240

87. Lansbury L, Leonardi-Bee J, Perkins W, et al (2010) Interventions for non-metastatic squamous cell carcinoma of the skin. Cochrane database Syst Rev 2015:CD007869. https://doi.org/10.1002/14651858.CD007869.pub2

88. Arazi L, Efrati M, Kelson I, Keisari Y (2012) Local control of experimental malignant pancreatic tumors by treatment with a combination of chemotherapy and intratumoral 224Radium-loaded wires releasing alpha-emitting atoms. Transl Res 159:32–41. https://doi.org/10.1016/j.trsl.2011.08.009

89. Domankevich V, Cohen A, Efrati M, et al (2019) Combining alpha radiation-based brachytherapy with immunomodulators promotes complete tumor regression in mice via tumor-specific long-term immune response. Cancer Immunol Immunother 68:1949–1958. https://doi.org/10.1007/s00262-019-02418-5

90. Bellia SSR, Feliciani G, Del Duca M, et al (2019) Clinical evidence of abscopal effect in cutaneous squamous cell carcinoma treated with diffusing alpha emitters radiation therapy: a case report. J Contemp Brachytherapy, https//doi.org/105114/jcb201988138 11:. https://doi.org/10.5114/jcb.2019.88138

91. Keisari Y, Kelson I (2021) The Potentiation of Anti-Tumor Immunity by Tumor Abolition with Alpha Particles, Protons, or Carbon Ion Radiation and Its Enforcement by Combination with Immunoadjuvants or Inhibitors of Immune Suppressor Cells and Checkpoint Molecules. Cells 10:228. https://doi.org/10.3390/cells10020228

92. Cooks T, Arazi L, Efrati M, et al (2009) Interstitial Wires Releasing Diffusing Alpha Emitters Combined With Chemotherapy Improved Local Tumor Control and Survival in Squamous Cell Carcinoma-bearing Mice. Cancer 1791–1801. https://doi.org/10.1002/cncr.24191

93. Arazi L, Cooks T, Schmidt M, et al (2010) The treatment of solid tumors by alpha emitters released from 224 Ra-loaded sources — internal dosimetry analysis. Phys Med Biol 55:1203–1218. https://doi.org/10.1088/0031-9155/55/4/020

94. Popovtzer A, Rosenfeld E, Mizrachi A, et al (2020) Initial Safety and Tumor Control Results From a “First-in-Human” Multicenter Prospective Trial Evaluating a Novel Alpha-Emitting Radionuclide for the Treatment of Locally Advanced Recurrent Squamous Cell Carcinomas of the Skin and Head and Neck. Int J Radiat Oncol Biol Phys 106:. https://doi.org/10.1016/j.ijrobp.2019.10.048

Acknowledgements

A special thanks to Professors Lior Arazi, Yona Keisari, and Itzhak Kelson for their assistance and the wonderful conversations we had together that enhanced the quality of the work presented in this thesis. In addition, I would like to express my gratitude to the Alpha Tau Medical LTD team for their immense enthusiasm and assistance in educating us on how to use DaRT technology. I hope that our productive collaboration will continue.